



EUROPEAN ORGANIZATION FOR NUCLEAR RESEARCH

CERN LIBRARIES, GENEVA



CM-P00045041

CERN/SPSC 84-31

CERN/SPSC/P199

May 22, 1984

A PROPOSAL TO MEASURE $\bar{\nu}_{\mu}$ -e SCATTERING
WITH A LARGE WATER CERENKOV DETECTOR^a

L. Behr², P. Bloch³, A. Blondel², J.M. Candelle³, J. Feltesse³,
R. Fries², F. Jacquet^{b, 2}, R. Kopp¹, R. Legac², D. Lellouch², A. Milsztajn³,
U. Meyer-Berkhout¹, A. Staude¹, M. Virchaux³, C. Zupancic¹

¹ Sektion Physik der Universität, Munich, Federal Republic of Germany

² École Polytechnique, Palaiseau, France

³ CEN, Saclay, France

^a Subject to Approval by the National Funding Agencies

^b Spokesman

ABSTRACT

We present a new method to perform a high statistics $\bar{\nu}_\mu e$ scattering experiment based on the detection of Cerenkov light emitted by forward produced electrons in a water target [1].

CONTENTS

Chapter	page
1. PHYSICS OBJECTIVES	3
Measurement of the Weinberg angle	3
Status of neutrino-electron scattering experiments	5
Search for rare processes	7
2. THE DETECTION PRINCIPLE	9
The inner detector	10
The forward detector	11
The shower scanner	12
Hadron rejection	13
3. EVENT SELECTION AND BACKGROUND REJECTION	15
Event selection	15
Background from $\bar{\nu}_\mu$ scattering on nuclei	16
Background from deep inelastic scattering	16
Coherent π^0 production	16
Background from interactions of electron neutrinos	17
$\bar{\nu}_e N$ interactions	17
$\bar{\nu}_e e$ interactions	18
Summary	18

4.	ERRORS ON THE MEASUREMENT OF $\text{SIN}^2\theta_W$	20
	Flux normalization	20
	Low Q^2 interactions	21
	Deep inelastic events in the muon spectrometer	21
	The neutrino flux monitor (NFM)	22
	The total cross-section ratio	22
	The differential cross section ratio	23
5.	EXPERIMENTAL SET-UP	25
	Layout	25
	Inner detector	26
	Forward detector	26
	Shower scanner	27
	Water tank and purification	27
	Muon detector	28
	Trigger, electronics and monitoring	29
	Running conditions	30
	Cost estimate	30
	REFERENCES	33
	FIGURE CAPTIONS	36

Chapter 1

PHYSICS OBJECTIVES

1.1 MEASUREMENT OF THE WEINBERG ANGLE

The $SU(2) \otimes U(1)$ model of electroweak interactions by Glashow, Salam and Weinberg is by now firmly established in lowest order perturbation theory, but tests of higher order predictions are still important to verify the renormalizability of the theory. One possible method is to measure at least two of the three quantities M_W , M_Z (the intermediate boson masses) and $\sin^2\Theta_W$ (the weak mixing angle) to high accuracy. The relation between these three quantities depends on the renormalization scheme; in the simplest case [2], $\sin^2\Theta_W = 1 - M_W^2/M_Z^2$. Born term calculations predict

$$M_Z \sin\Theta_W \cos\Theta_W = 37.3 \text{ GeV}$$

while in order α , this relation becomes [3]

$$M_Z \sin\Theta_W \cos\Theta_W = 37.3 \text{ GeV} \cdot (1 + \Delta r)$$

where $\Delta r = 0.032$ for a Higgs boson mass $M_H = M_Z$ and a top quark mass $M_t = 20 \text{ GeV}$. Δr depends slightly on the Higgs mass and varies from 0.030 to 0.037 for $10 < M_H < 800 \text{ GeV}$. It is insensitive to the top quark mass as long as $M_t < 80 \text{ GeV}$; for large values of M_t , Δr is dominated by a negative term quadratic in M_t and amounts to -0.03 for $M_t = 300 \text{ GeV}$.

Assuming that e^+e^- collider experiments will measure the Z^0 mass with negligible errors and that $M_t < M_Z$, a measurement of $\sin^2\Theta_w$ with an error of 0.005 provides a test of order α corrections predicted by renormalizable electroweak gauge models at the 4σ level. This precision is achieved most safely in $\nu_\mu e$ elastic scattering which is a purely leptonic process free of theoretical uncertainties due to strong interaction dynamics.

The differential cross sections

$$\frac{d\sigma}{dy}(\nu_\mu e \rightarrow \nu_\mu e) = \frac{2}{\pi} G^2 m_e E_\nu [g_l^2 + g_r^2 (1-y)^2] \quad (1a)$$

$$\frac{d\sigma}{dy}(\bar{\nu}_\mu e \rightarrow \bar{\nu}_\mu e) = \frac{2}{\pi} G^2 m_e E_\nu [g_l^2 (1-y)^2 + g_r^2] \quad (1b)$$

where G is the Fermi constant, m_e the electron mass, E_ν the neutrino energy and $y = E_e/E_\nu$, depend on the coupling constants g_l and g_r which in the standard model are

$$g_l = -1/2 + \sin^2\Theta_w \quad (2a)$$

$$g_r = \sin^2\Theta_w \quad (2b)$$

The ratio of the total elastic cross sections,

$$R = \sigma(\bar{\nu}_\mu e) / \sigma(\nu_\mu e) \quad (3)$$

is well known to be very sensitive to $\sin^2\Theta_w$: for $\sin^2\Theta_w = 0.21$, $\Delta\sin^2\Theta_w = 1/8 \Delta R$. Moreover, it is evident from (1) that the ratio of differential cross-sections is insensitive to $\sin^2\Theta_w$ at small y , whereas a shift of 0.005 of $\sin^2\Theta_w$ corresponds to a 8.5% shift of the cross-section

ratio for $y > 0.9$ (fig. 1). Therefore, a measurement of the y distribution provides an independent determination of $\sin^2\Theta_W$ to improve the overall accuracy.

A measurement of $\sin^2\Theta_W$ from a cross-section ratio presents two clear advantages:

1. Experimental uncertainties from the cut on the electron energy and detector inefficiencies cancel.
2. Radiative corrections cancel as well and $\sin^2\Theta_W$ extracted from equation (1) differs by only 0.0005 [4] from $\sin^2\Theta_W$ defined by $\sin^2\Theta_W = 1 - M_W^2/M_Z^2$;

1.2 STATUS OF NEUTRINO-ELECTRON SCATTERING EXPERIMENTS

Neutrino-electron scattering is distinguished by two prominent characteristics:

1. The cross-section is very small ($\sigma \approx E_\nu \cdot 10^{-42}$ cm²/GeV, which is about 10^{-4} of the ν_μ -nucleon cross-section) and a high mass detector is required to obtain sufficient statistics;
2. the angle of the scattered electron with respect to the neutrino direction is small:

$$\Theta_e = \sqrt{(2m_e/E_e)(1-y)} \leq 32\text{mrad}/\sqrt{E(\text{GeV})} \quad (4)$$

and a good angular resolution is necessary to separate well signal and backgrounds and to minimize systematic errors.

Bubble chambers have a good angular resolution but yield only poor statistics due to their low target mass, typically a few tens of events.

The calorimeter of the CHARM I collaboration [5] uses a moderate fiducial mass of 80 t and has an angular resolution which is larger than the kinematical limit (4), entailing a large uncertainty on the background subtraction. The fine grain calorimeter of the Brookhaven neutrino detector has a fiducial mass of 80 t of liquid scintillator and a resolution of 22 mrad/ \sqrt{E} but is exposed to the low energy neutrino beam of the Brookhaven AGS ($\langle p_\nu \rangle = 1.4$ GeV) [6]. The results of these two experiments are summarized in table 1. At the end of their analysis, the BNL experiment expects 150 ν_μ and 90 $\bar{\nu}_\mu$ events and an error on $\sin^2\theta_w$ between 0.01 and 0.015 [7].

TABLE 1

Results of the most recent experiments

	S/B	# PROTON ON TARGET		# ν_μ e evt	# $\bar{\nu}_\mu$ e evt	$\sin^2\theta_w$	$\Delta(\sin^2\theta_w)$	Ref.
		ν BEAM	$\bar{\nu}$ BEAM					
BNL(734)	2/1	$2.9 \cdot 10^{19}$	$3.6 \cdot 10^{19}$	13 (1981) 51 ± 3 $\sim 1/3$ data	44 ± 12 $\sim 1/2$ data Preliminary	(3)	(3)	[7]
CHARM 1	1/2	$1.4 \cdot 10^{18}$	$5.7 \cdot 10^{18}$	46 ± 12	77 ± 19	0.215	$\pm 0.040 \pm 0.015$	[9]

A straightforward method to reduce the errors further is to build a larger calorimeter with fine grain. The CHARM II calorimeter will have a fiducial mass of 436 t and an angular resolution of 16 mrad/√E. With $5 \cdot 10^{18}$ protons on target for neutrinos and $1 \cdot 10^{19}$ protons on target for antineutrinos they expect an accuracy on $\sin^2 \Theta_w$ of 0.005 [8].

Here, we propose a different approach which combines a comparable fiducial mass with an angular resolution five times better than the kinematical limit.

1.3 SEARCH FOR RARE PROCESSES

Beyond the test of higher order corrections to the standard model, the proposed apparatus offers a variety of possibilities to study other processes, exploiting the good sensitivity of the detector to low Q^2 and low mass reactions. Also, it will be possible to study in detail the structure function of the nucleon for very low x ($x < 0.01$).

The inverse muon decay $\nu_\mu e \rightarrow \mu^+ \nu_e$ gives limits on the right handed helicity of the neutrino assuming V-A interaction, or on the V+A component of the charged current when assuming left-handed neutrinos. For this reaction we expect 20 times more statistics than collected in earlier experiments [9]. The good $e/\gamma/\pi^0$ identification will allow us to study rare decay modes like $\nu_\mu \rightarrow \nu_e e^+ e^-$, axion $\rightarrow \gamma\gamma$, etc. at a mass scale of few hundred MeV [10].

Another important physics objective is the search for new gauge bosons. In supersymmetric theories, the extension of the standard gauge group to $SU(2) \otimes U(1) \otimes U(1)$ implies the existence of a second neutral gauge boson U [11] which is predicted to be light. The existence of such a boson changes the couplings (2) to

$$g_l = -\frac{1}{2} + \sin^2 \theta_w + \frac{1}{8}(1 - \cos \phi_\mu)(1 - \cos \phi_e) \frac{M_U^2}{M_U^2 + Q^2}$$

$$g_r = \sin^2 \theta_w + \frac{1}{8}(1 - \cos \phi_\mu)(1 + \cos \phi_e) \frac{M_U^2}{M_U^2 + Q^2}$$

where ϕ_μ and ϕ_e parametrize the vector coupling of the e and μ currents to the U. This modification of the standard values of g_l and g_r leads to appreciable changes of the cross-sections (1) for $Q^2 < M_U^2$. As an example, assuming $\cos\phi_e = 0$, $\cos\phi_\mu = -1$ and $\sin^2\theta_w = 0.25$, the number of events observed for $Q^2 < M_U^2$ is only 1/4 of the standard value and a Q^2 analysis of the reaction will allow us to set limits on the U mass.

Chapter 2

THE DETECTION PRINCIPLE

The proposed detector is designed around a large volume of water which serves both as target and as Cerenkov radiator. The Cerenkov light emitted by charged particles travelling in water is detected by three complementary methods which combine angle and energy measurement with a good electron identification. A veto-counter in front and a downstream muon spectrometer complete the apparatus.

A $\beta = 1$ particle in water gives rise to a Cerenkov light cone with a half-opening angle of 42 degrees. This light, detected by photomultipliers, yields an average number of 20 photoelectrons per track per cm. This number has been checked experimentally [12] and includes the quantum efficiency of a standard photomultiplier (PM) and the loss due to UV absorption in water and in a plastic window. The idea to use this Cerenkov light to measure the electron angle has been put forward originally by Cronin and Swartz [13]. In their proposal, the Cerenkov cone is detected through two tilted opposite windows. A small deviation from the forward direction is measured comparing the amount of light traversing the two windows. This method obviously suffers from correlations between angle and energy measurement.

We propose three independent measurements of the Cerenkov light:

1. The "inner detector", similar to the IMB proton lifetime detector, measures the total energy deposited with an array of hemispherical phototubes installed in the water and gives some pattern information;

2. The "forward detector" measures the Cerenkov cone through the water surface with a system of spherical mirrors which focus the light on an array of phototubes, giving a very precise measurement of the electron angle and another estimate of the energy, the forward energy E_f ;
3. The "shower scanner", a system of angle selective photon detectors, measures the amount of light produced in $1/3 X_0$ thick transverse slices to observe the longitudinal development of electromagnetic showers.

To establish the performance of the forward detector and the shower scanner, we have carried out a test with a small scale prototype detector in the CERN SPS X5 test beam in december 1983, using a water tank with a volume of $4.4 \times 1.5 \times 1.0 \text{ m}^3$.

2.1 THE INNER DETECTOR

The inner detector consists of a set of photomultipliers which are installed in the water and distributed around the fiducial volume in a regular array. With two photomultipliers per square meter, collecting light over a wide angular range, we obtain a coverage of 3% and expect a resolution of $\sigma_E/E = 10\%/VE$ for electromagnetic and $\sigma_E/E = 50\%/VE$ for hadron showers. By pattern analysis, the inner detector also provides a measurement of the shower position with a resolution of $\approx 10 \text{ cm}$.

2.2 THE FORWARD DETECTOR

A section of the Cerenkov light cone emitted by a small straight segment of a charged track leaves the tank through the surface of the water. The image of this part of the cone generated in the focal plane of the spherical mirror is, to first approximation, an arc of a circle. The following track segment, if it has the same direction as the preceding one, gives the same picture in the focal plane; there is an unambiguous relation between the impact point on the focal plane and the direction of the photon in the water, independent of the emission point (fig. 2). A change of the photon direction by 1 mrad in a plane perpendicular to the water surface is amplified by the refraction to a change of 4 mrad in the outside air, reducing the quality requirements on the external optics accordingly.

The measurement in the focal plane gives a precise measurement of the projected angle Θ_z of the track in a plane perpendicular to the water surface. The forward detector is designed to accept Cerenkov photons emitted by tracks in an angular range of $-30 \text{ mrad} < \Theta < 60 \text{ mrad}$ with respect to the beam axis.

A measurement of the angular resolution was an important aim of the prototype test (fig. 3). The forward detector was made of three spherical mirrors of $80 \times 80 \text{ cm}^2$ each and a focal length of $\approx 6 \text{ m}$. The focal plane was instrumented with 105 photomultipliers EMI 9814KB, each equipped with an aluminized mylar light guide for better light collection, covering a total surface of $90 \times 90 \text{ cm}^2$. For muon tracks, we observe a very clear ring signal (fig. 4), showing up as a peak in the photon angular distribution with almost no background. For 20 GeV muons, we find a RMS angular resolution better than 1.5 mrad, which is degraded towards lower energies by multiple scattering in the water. For electron tracks, the peak is still visible event by event (fig. 5), but shows up on top of a much wider distribution which reflects the angular spread of the secondaries in the electromagnetic shower. The shower retains the direction of the primary electron down to energies as

low as 2 - 3 GeV. The electron angle is determined either from the peak of the projected photon distribution or by fitting the data with a parametrization of the angular distribution determined from a Monte Carlo simulation. The resulting electron angular resolution does not behave gaussian (fig. 6). We characterize it by two numbers, $\sigma = \text{FWHM}/2.3$ which is $\sigma = 6\text{mrad}/\sqrt{E}$, and by the fraction r of events outside a 2σ cut; r increases with decreasing energy and varies between 10% for 20 GeV and 33% for 3 GeV electrons (fig.7).

For the measurement of the forward energy, the number of photoelectrons PE was found to be proportional to the electron energy; it is 47 PE/GeV for the acceptance of ± 20 mrad of the prototype detector (fig. 8). The corresponding energy resolution is $\sigma_E/E = 0.3/\sqrt{E}$ and is limited both by photostatistics and by shower fluctuations.

Finally, we observe that the shape of the peak in the focal plane close to the maximum is different for electrons, muons and pions, providing important information for background rejection (figs. 4, 5 and 9).

2.3 THE SHOWER SCANNER

Gamma rays from various sources are expected to be a major background as well as a signature for a variety of unconventional phenomena. For both reasons, a good separation of photons from electrons is of crucial importance. They can be distinguished only in the initial development phase of the shower from the different number of Cerenkov photons emitted along the first fraction of a radiation length of the track. In the subsequent shower development, a large number of wide angle tracks is produced, emitting a halo of Cerenkov light which contributes to the total energy measurement but deteriorates the information about the beginning of the track when the shower is observed with the inner detector. Therefore, we will measure the Cerenkov photons

in bins of short segments along the beam direction. The "shower scanner" is made of four rows of PMs and detects photons emitted by tracks within a small angle around the beam axis in intervals of $\frac{1}{3} X_0$.

The shower scanner of the prototype was made of 2x21 photomultipliers of type Philips XP 2020, arranged in seven columns of three tubes each on both sides of the tank (fig. 3). We have measured the profile of showers induced by pions, electrons and converted γ rays along the first radiation length of the water volume. Their patterns can be clearly distinguished. A selection on an event-by-event basis can be achieved with appropriate cuts on the number of photo-electrons observed in the photomultiplier columns viewing the origin of the shower (fig. 10). We have investigated the e/ γ separation for various cuts in various distances from the shower origin. With a sampling every $\frac{1}{3} X_0$, it is possible to retain 80% of the electrons with a γ rejection of a factor 5 (fig. 11).

In addition, we find that the shower scanner can determine, by comparison of the total number of photoelectrons measured in each row, the position of the interaction vertex with an accuracy of ≈ 10 cm.

2.4 HADRON REJECTION

We have not verified the rejection of hadron showers from neutrino interactions directly with the test detector. However, we have checked the different responses of the focal plane to showers from single pions and electrons of given energies, which are essential inputs for any background calculation. The rejection is mainly achieved by comparing the total energy (which will be measured by the inner detector in the experiment) to the forward energy measured in the focal plane. A 10 GeV pion fakes a 10 GeV electron for only $5 \cdot 10^{-3}$ of the events (fig. 12).

In addition, the shape of the photon distribution in the focal plane, characterised roughly by the ratio of the peak height E_{peak} to the forward energy E_f gives an additional rejection factor .

Finally, the analysis of the longitudinal shower profile observed in the shower scanner improves the rejection to better than 10^{-3} .

Chapter 3

EVENT SELECTION AND BACKGROUND REJECTION

3.1 EVENT SELECTION

The signature of $\bar{\nu}_\mu e$ events is a single electron emitted under an angle $\Theta_e < 32 \text{ mrad}/\sqrt{E}$ with respect to the neutrino direction, which is within the acceptance of the forward detector for electron energies greater than 2 GeV. We recall briefly the principal characteristics of the forward single electron signal which we expect to observe and which have been confirmed by the test beam measurements:

1. The energy E_f measured in the forward detectors has to agree with the total energy E_t within the combined resolutions of the two measurements. We intend to accept events where E_f/E_t lies within 2 standard deviations around the expected value.
2. In the forward detector, the photon distribution must exhibit the shape which is characteristic for electron events, corresponding to a specific ratio of peak energy to total energy E_f .
3. No muon must be detected in the muon spectrometer or in the Cerenkov detector.

In order to optimize the signal/background ratio, we will use only electrons in the energy range 5-30 GeV. In addition, we require that the electron stays within the kinematic limit. Accepting events with $E\Theta^2 < 1.2 \text{ MeV}$, we retain 85% of the electrons in the above energy range.

3.2 BACKGROUND FROM $\bar{\nu}_\mu$ SCATTERING ON NUCLEI

3.2.1 Background from deep inelastic scattering

This process occurs $\approx 10^4$ times more frequently than our signal. Its rejection is based on the efficient discrimination between hadronic and electromagnetic showers and on the much wider angular spread of hadronic events observed in the forward detector. The majority of charged current events are identified through the final state muon.

The probability that a hadronic shower of energy E_h , emitted under an angle Θ_h with respect to the beam, fakes a $\bar{\nu}_\mu e \rightarrow \bar{\nu}_\mu e$ event accepted by the selection criteria was estimated by a Monte Carlo simulation [14]. The program was carefully tuned to reproduce both our test beam data and neutrino production data. We find a probability

$$P(E_h, \Theta_h) = 2.6 \cdot 10^{-3} \exp(-E_h/6.2 \text{ GeV}) \exp(-\Theta^2/.035^2);$$

integrated over the accepted kinematic range, this corresponds to a rejection factor of $7 \cdot 10^{-6}$ for neutrino and $5 \cdot 10^{-6}$ for antineutrino induced neutral current events. We estimate similar rejection factors for charged current reactions where the muon is not detected ($E_\mu < 3$ GeV).

3.2.2 Coherent π^0 production

This important source of background was not estimated in our earlier letter of intent. It generates forward π^0 's with a broad $E\Theta^2$ distribution ($\sigma \approx 50$ MeV at $E_{\pi^0} = 20$ GeV) [15]. Data reported recently by a low energy neutrino experiment [16] are in satisfactory agreement with calculations by Rein and Sehgal [15].

Using the formulae of ref. [15], we have evaluated the π^0 background in our experiment. About 50% of these events are rejected by the cuts on the forward detector due to a large opening angle of the γ pair. The remaining background will be studied by selecting γ 's (i.e. large signals in the first radiation length of the shower) in the monitor region $3 < E\theta^2 < 60$ MeV. and extrapolating into the signal region for statistical subtraction.

3.3 BACKGROUND FROM INTERACTIONS OF ELECTRON NEUTRINOS

3.3.1 $\bar{\nu}_e N$ interactions

$\bar{\nu}_e N$ neutral current interactions, and charged current interactions in which the electron misses the forward detector, are rejected with the same efficiency as usual $\bar{\nu}_\mu N$ neutral current events. These events amount to only 1.9% (2.6%) of $\nu_\mu N$ ($\bar{\nu}_\mu N$) interactions and can be neglected. A much more important background arises from $\bar{\nu}_e N$ charged current interactions where the final state electron gives a signal in the forward detector, but the associated hadronic energy is too low to affect the E_f/E_t balance. To this background contribute mainly quasielastic $\bar{\nu}_e N \rightarrow e^- N$, Δ production $\bar{\nu}_e N \rightarrow e^- \Delta$, and low inelasticity interactions.

Since $\bar{\nu}_e$'s from kaon decays have a much higher energy than the muon neutrinos in the wide band beam, this background is concentrated at high electron energies. The cut $E_e < 30$ GeV will reduce it to less than 25%. The $E\theta^2$ distribution of this background is broad. Its integral amount can be determined by selecting clean electrons in the monitor region with help of the shower scanner; its shape is evaluated from low Q^2 $\bar{\nu}_\mu N \rightarrow \mu^+ X$ data, replacing the μ by an electron by a Monte Carlo procedure and applying the electron selection criteria. We expect $> 10^4$ quasielastic ν_μ interactions in the accepted kinematic range ($5 \leq E_\mu \leq 30$ GeV, $E_\mu \theta_\mu^2 < 1.2$ MeV), which is sufficient to estimate this

background. ν_μ data can only be used below the energy threshold for inverse β decay.

3.3.2 $\bar{\nu}_e$ interactions

Charged and neutral current $\bar{\nu}_e$ interactions are indistinguishable from $\bar{\nu}_\mu$ interactions and can only be subtracted statistically. The $\bar{\nu}_e$ cross section, being ≈ 6 times higher than the $\bar{\nu}_\mu$ cross-section, contributes $\approx 10\%$ to the ν_μ and 6.5% to the $\bar{\nu}_\mu$ sample. These rates decrease to about 7.5% resp. 4.2% in the $E\Theta^2 < 0.4$ MeV region which we use for the subsequent γ analysis.

The $\bar{\nu}_e$ flux must therefore be known to an accuracy of $\approx 15\%$. It can be monitored by selecting $\bar{\nu}_e N$ interactions in the background region, using the shower scanner to distinguish these reactions from coherent π^0 production.

3.4 SUMMARY

Table 2 and figs. 13-16 summarize the signal and background evaluations. We have assumed a fiducial mass of 400 t and exposures of $5 \cdot 10^{18}$ protons on target for neutrinos and 10^{19} for antineutrinos.

Note that in this table we have not used the e/ γ separation from the shower scanner. A cut which retains 80% of the electrons reduces the photon background by a factor of 5.

TABLE 2

Summary of background estimates

Channel	Nr. of events in signal region $E\theta^2 < 1.2 \text{ MeV}$	Nr. of events in monitor region $3 < E\theta^2 < 60 \text{ MeV}$
$\nu_{\mu}e$	1355	
$\nu_{\mu}N \text{ CC}$	50	
$\nu_{\mu}N \text{ NC}$	55	5000
Coherent π^0	310	
$\nu_e N$	220	3500
$\nu_e e$	129	
Total	2119	
$\bar{\nu}_{\mu}e$	1332	
$\bar{\nu}_{\mu}N \text{ CC}$	20	
$\bar{\nu}_{\mu}N \text{ NC}$	40	4850
Coherent π^0	310	
$(\nu_e + \bar{\nu}_e)N$	450	9500
$(\nu_e + \bar{\nu}_e)e$	87	
Total	2239	

Chapter 4

ERRORS ON THE MEASUREMENT OF $\sin^2\theta_W$

As discussed before, $\sin^2\theta_W$ can be evaluated both from the total cross-section ratio $\sigma(\bar{\nu}_\mu e)/\sigma(\nu_\mu e)$ and, with better systematic accuracy, from the ratio of the differential cross-sections (1) at large y . A knowledge of the incoming muon flux is needed in both cases.

4.1 FLUX NORMALIZATION

The energy spectrum of the incoming beam can be measured via a study of low Q^2 $\nu_\mu N$ interactions, mainly quasielastic events and resonance (Δ , Σ , ...) production. The Q^2 of these events must be larger than ≈ 0.08 GeV^2 to eliminate the inverse muon decay channel and to exclude the Q^2 range where Pauli suppression becomes important. The cross-sections for these reactions are energy independent. Uncertainties arising from the absolute calibration of the muon energy ($\approx 2\%$) and the momentum resolution cancel to a large extent in the $\bar{\nu}_\mu/\nu_\mu$ flux ratio and can be controlled to a level of $< 2\%$.

To measure the flux ratio, we have three different methods at our disposal:

4.1.1 Low Q^2 interactions

At small Q^2 , ν_μ and $\bar{\nu}_\mu$ cross-sections differ by an interference term which goes to 0 at $Q^2 = 0$ and which can be computed with an accuracy of 0.5% for quasielastic reactions and 2.5% for Δ production [17], provided Q^2 is smaller than 0.15 GeV^2 . In our experiment, ν_μ and $\bar{\nu}_\mu$ interaction rates will also be different due to the presence of free protons in water. Quasielastic neutrino reactions occur on bound neutrons, whereas antineutrino reactions occur, in a proportion 1:4, on free and bound protons for which the cross-sections at low Q^2 are different due to Pauli suppression. The Pauli suppression factor has been estimated with various nuclear models and found to be 0.9 ± 0.1 in this Q^2 range.

To the elastic events we have to add a contribution from resonance production. These reactions are effectively not Pauli suppressed but have different cross-sections for protons and neutrons, entailing another systematic difference in the ratio of neutrino to antineutrino interaction rates in water.

These theoretical uncertainties cancel only partially in the $\bar{\nu}/\nu$ ratio and lead to a systematic uncertainty of $\approx 4\%$ in the relative flux normalization.

4.1.2 Deep inelastic events in the muon spectrometer

The CDHS experiment will measure, during the 1984 narrow band exposure, the ratio of total neutrino to antineutrino cross-sections in the energy range 20-50 GeV with an expected accuracy better than 4% [18]. Using the muon spectrometer as target, and applying the same trigger, calibration procedure and analysis criteria as the present CDHS experiment, we can monitor the flux ratio in this energy range with the same systematic accuracy.

4.1.3 The neutrino flux monitor (NFM)

In the NFM, muon fluxes are measured in the μ shielding at several penetration depths and in various distances from the beam axis with solid state detectors [19]. This facility is expected to provide another measurement of the $\bar{\nu}/\nu$ ratio to better than 4% [20], since systematic errors of the absolute flux measurement cancel again to a large extent. The remaining error arises mainly from uncertainties on the π/K ratio (1.5%), wrong sign muons which contribution can be measured in the experiment (1%), and inefficiencies of the solid state detectors which can be monitored during the run (0.5%).

In summary, we expect to have three independent measurements of the $\bar{\nu}/\nu$ flux ratio with a systematic accuracy $\leq 4\%$ each.

4.2 THE TOTAL CROSS-SECTION RATIO

Table 2 summarizes the number of events for the $\bar{\nu}_\mu e/\nu_\mu e$ sample. The statistical error of the cross section ratio $R = \sigma(\bar{\nu}_\mu e)/\sigma(\nu_\mu e)$ is $\Delta R/R = 4.9\%$. This error increases by only 0.4% if the background subtraction accounting for $\nu_\mu N$ interactions increases by a factor of 2. Also, systematic uncertainties in the background subtraction cancel to a large extent in the $\bar{\nu}_\mu/\nu_\mu$ ratio.

The principal source of systematic errors is the relative flux normalization. Assuming a 4% error on the relative flux normalization, we obtain

$$\Delta \sin^2 \Theta_w = 0.0055 \text{ (stat.)} + 0.0045 \text{ (syst.)}$$

4.3 THE DIFFERENTIAL CROSS SECTION RATIO

The excellent angular resolution of our detector allows us to extract additional information from the $y = 1 - E\Theta^2$ distribution. As discussed in chapter 1, the sensitivity of the differential cross-section ratio to $\sin^2\Theta_w$ increases towards large y ; the loss of statistics due to selection of high y events is compensated by the increase in sensitivity, while systematic errors from the relative flux normalization become less important.

The experimental resolution in the interval $0.6 \leq y \leq 1.0$ is $\sigma_y = 0.3$; therefore, a cut $y > 0.6$ selects events with an average true y $\langle y^{\text{true}} \rangle = 0.66$. A change of $\sin^2\Theta_w$ by 0.005 corresponds to a shift of the restricted ratio

$$R' = \frac{\int_{y>.6} \frac{d\sigma}{dy} (\bar{\nu}_\mu e) dy}{\int_{y>.6} \frac{d\sigma}{dy} (\nu_\mu e) dy}$$

by 6.7% (instead of 4.5% for R).

Table 3 gives the expected number of signal and background events for $y \geq 0.6$.

The statistical error of R' is $\Delta R'/R' = 0.076$, corresponding to a statistical error $\Delta \sin^2\Theta_w = 0.0055$. A 4% error on the flux ratio gives rise to a change $\Delta \sin^2\Theta_w = 0.0033$ only and a 20% error on the resolution function will affect the result by not more than 0.001.

More sophisticated approaches are to fit the cross-section ratio in bins of y or to perform a maximum likelihood on the ratio of the y distributions. These methods, using no information on the relative flux

TABLE 3

Expected number of events for $y \geq 0.6$

Neutrinos		Antineutrinos	
ν_e	579	$\bar{\nu}_e$	541
ν_μ	35	$\bar{\nu}_\mu$	20
coh. π^0	100	coh. π^0	100
$\nu_e N$	73	$(\nu_e + \bar{\nu}_e) N$	150
$\nu_e e$	47	$(\nu_e + \bar{\nu}_e) e$	23

normalization, yield a measurement of $\sin^2\Theta_W$ with a statistical error $\Delta\sin^2\Theta_W = 0.013$.

Using all the information, including the relative flux normalization, we obtain a final error of $\Delta\sin^2\Theta_W = 0.005$.

Chapter 5

EXPERIMENTAL SET-UP

5.1 LAYOUT

The design of the detector is based on a fiducial mass of 400 tons, corresponding to a volume of 10 m^2 cross-section \times 40 m length.

The forward detector is designed to measure the vertical and the horizontal component of the electron direction. The water surface serves as exit window for both components; for the horizontal measurement, the light is reflected by a planar mirror installed inside the water tank under an angle of 45 degrees. Both the vertical and the horizontal detector are segmented in 5 modules 9 m long each to minimize the total surface of the spherical mirrors (fig. 17).

The shower scanner is designed to sample the emitted Cerenkov light every $\approx 1/3$ of a radiation length (14 cm), viewing the total fiducial volume with 4 phototubes per $1/3 X_0$ slice.

The total energy measurement is designed to achieve a 3% coverage with a regular array of photomultipliers (fig. 18).

5.1.1 Inner detector

The fiducial volume is viewed, over a cross section of $4 \times 4 \text{ m}^2$ and a length of 45 m, by 1000 hemispherical phototubes arranged on a $.8 \text{ m} \times .7 \text{ m}$ grid. The glass window of the PMs is in direct contact with the water, whereas the body of the PM and the base are enclosed in a sealed PVC pipe. A single cable carries the supply voltage and the output signal. Tubes and bases are attached to the tank with strings of nylon filament. Fig. 19 [21] shows the set-up used by the IMB collaboration.

5.1.2 Forward detector

The forward detector consists of a large planar mirror inside the water and 2×5 detection modules. Each module is made of a spherical mirror and a detection plane which coincides with the focal plane of the mirror.

The planar mirror installed in the water has a size of 300 m^2 and is composed of individual mirrors 2 m^2 large. Each of them is made of two flat glass plates glued to a light support in between which is chosen to result in a total density close to 1 g/cm^3 .

Each of the spherical mirrors covers an area of 7 m (horizontal) by 3 m (vertical) and will be assembled of units of $75 \times 75 \text{ cm}^2$ size.

To cover an acceptance of $-30 \leq \Theta_z \leq 60 \text{ mrad}$ in polar angle and 200 mrad in azimuth, the detectors in the focal plane have to be 1.60m wide and 2.10m high. Each of them is instrumented with 140 2" photomultipliers which are equipped with conical light-guides to match the area covered by each of them to the resolution of the optical system.

5.1.3 Shower scanner

The shower scanner is made of four horizontal rows of photomultipliers viewing the fiducial volume from four corners along the beam direction. Each PM is equipped with a light collector which serves a twofold purpose, namely (i) to select photons emitted by a limited segment of the track along the beam direction, and (ii) to integrate over the azimuth angle ϕ . This device is sketched in fig. 20.

5.2 WATER TANK AND PURIFICATION

To provide space for the mirror which reflects the horizontal view of the Cerenkov cones upwards, the total width of the tank has to be substantially larger than the fiducial width. The tank is 14 m wide, up to 8 m deep and 50 m long and contains 2600 m³ of water. It is built out of concrete which on the inside is covered with PVC foils.

The average light path inside the water is 6 m for the direct (vertical) and 15 m for the reflected (horizontal) view. A standard purification system similar to the IMB one [22] is largely sufficient to guarantee an adequate attenuation length.

5.3 MUON DETECTOR

A muon spectrometer is installed downstream of the water tank, mainly for flux monitoring by measuring final state muons from low Q^2 interactions of the type $\nu_{\mu} N \rightarrow \mu X$ in the water (cf. section 4.1). We will also use the upstream part of the muon spectrometer as target, taking advantage of the fact that the ratio of $\bar{\nu}/\nu$ cross sections in iron will have been measured by then with good accuracy [18]. This will give us a completely model independent cross-check on the relative normalization of the ν fluxes.

We intend to use 7 old type modules from the CDHS spectrometer, the first 4 with fine and the last 3 with coarse segmentation. This arrangement allows to use the second module as a target. The diameter of the modules (3.75m) matches their acceptance to the fiducial volume of the water at least for low Q^2 events.

These modules should be fully equipped with scintillators, phototubes with associated electronics, and the drift chambers. We would also like to install two drift chambers behind the last module separated by 1 m. Knowing the direction of the muon track in the water and behind the iron toroids, we can achieve a momentum resolution better than 10% over the relevant energy range.

5.4 TRIGGER, ELECTRONICS AND MONITORING

The trigger decision will be split in two levels. A fast hardware logic, which gives a primary trigger rate of ≈ 100 triggers/burst, is based on analog sums of PM signals and has three main components:

1. An inner detector trigger requiring $E_t > E_0$;
2. a focal plane (forward detector) trigger requiring $E_f > E_0'$;
3. a shower scanner trigger requiring a minimum shower length $l > l_0$.

ORing of the three first level triggers will allow to cross-check their efficiencies amongst each other.

The second level trigger will be used to select $\nu_\mu e$ candidates and to sample events of various types for calibrations. This can be:

1. a hardware trigger, using the information of the first level triggers and a rough comparison of E_f to E_t , with which we expect to lower the trigger rate to less than 5 events per burst. In this case, we could use standard fast ADC's (with 12 bits and 500 nsec conversion time) in a multiplexed mode.
2. A software trigger, based e.g. on CAMAC booster processors (CABs). The CABs allow to process 100 events in 2 sec. In this case, the analog-to-digital conversion will use charge integrators and analog multiplexors coupled to 8 bit 20 MHz flash ADCs. Two output channels with different conversion scales provide a dynamic range of 1:2000. Multiplexing reduces the number of ADCs needed. The deadtime will be about 500 nsec.

Between bursts we will take events for monitoring of the electronics and optics. Changes of detector responses will be detected immediately.

The relative calibration of the phototubes is done with a laser pulse [24] which is distributed by optical fibres to light diffusing spheres [23]. The response of the tubes can also be determined with the single photoelectron peak.

The absolute calibration is done with muons and with electrons which we intend to send from the West Area electron test beam into our detector.

5.5 RUNNING CONDITIONS

The detector will be operated at the SPS wide band neutrino beam. An integrated luminosity of $1.5 \cdot 10^{19}$ protons on target, with a $\bar{\nu}$: ν sharing of about 2:1, is needed to obtain a statistical error of 0.005 on $\sin^2\Theta_W$. The place which is best suited to install the detector is the BEBC experimental hall as shown in fig. 17.

We foresee a construction time of 2 years and expect to be ready for SPS fixed target operation in 1987.

5.6 COST ESTIMATE

Table 4 summarizes the anticipated cost of the experiment, not including the muon spectrometer, on-line computers and the preparation of the BEBC Hall. For all items where the technical realization has not yet been finalized we give upper and lower limits only.

Since we are still in discussions with other institutes about a possible extension of the collaboration, the sharing of work and costs has not yet been decided. For this, we intend to submit an addendum to this proposal at a later date.

TABLE 4

Cost estimates for the proposed detector

	Cost in MSF
Water tank and purification	
Water tank	.3 - .5
PVC foils	.06
Purification system	.10 - .25
Plastic roof	.26
Mirrors	
Spherical mirror 230 m ² (2500 SF/m ²)	.575
Main support	.25 - .35
Individual supports (adjustable)	.12 - .23
Underwater mirror	.24
Adjustable supports	.12 - .23
Inner detector	
PM supports	.03
1000 5" PMs with PVC pipes	.47
Focal plane detector	
PM supports	.03
1400 2" PMs with Mylar reflectors	.31
Shower scanner	
1260 5" PMs with PVC pipes	.59
1260 reflectors	.25 - .33
Electronics	
3660 bases	.07
3660 HV channels	.20
3660 cables, integrators, ADCs	.50 - .67
Crates	.03
Trigger electronics	.03 - .07
Anticounter system	.03
 Total	 4.57 - 5.53

REFERENCES

1. P. Bloch et al., "An experiment to measure $\nu_{\mu}e$ scattering with a large water Cerenkov detector", CERN/SPSC/1146 (CERN-SPSC 83-44) (Letter of Intent)
2. A. Sirlin, Phys. Rev. D22, 971 (1980); W. J. Marciano and A. Sirlin, Phys. Rev. D22, 2695 (1980).
3. For a general review on higher order effects see, for instance, M. Consoli, S. Lo Presti and L. Maiani, preprint PP/738-14/1/1983, Catania 208; C.H. Llewellyn Smith and J.F. Wheeler, Nucl. Phys. B208, 27 (1982).
4. D.Yu. Bardin and V.A. Dokuchaeva, to be published in Sov. Jad. Phys.
5. F. Bergsma et al., Phys. Lett. 117B, 272 (1982).
6. L.A. Ahrens et al., Phys. Rev. Lett. 51, 1514 (1983).
7. R.E. Lanou, Proc. XIXth Rencontre de Moriond, J. Tran Thanh Van ed. (1984), to be published.
8. CHARM II Proposal, CERN/SPSC/83-24 (April 1983).
9. F. Bergsma et al., Phys. Lett. 122B, 465 (1983).
10. F. Vanucci et al., Proposal CERN/PSCC 83-13 (1983).

11. P. Fayet, Proc. XVIIth Rencontre de Moriond, Vol. 1, p. 483 (1982), J. Tran Thanh Van ed.
12. L. Behr et al., Nucl. Instr. Meth 190, 5 (1981).
13. J. W. Cronin and M. L. Swartz, Fermilab Proposal 600 (May 1978).
14. A. Blondel and F. Jacquet, Nucl. Phys. 117B, 115 (1982); program CASCAD, courtesy of A. Grant, CERN.
15. D. Rein and L. M. Sehgal, preprint Aachen (1982) and Nucl. Phys., to be published.
16. H. Faissner et al., Phys. Lett. 125B, 230 (1983).
17. Addendum to the CHARM II Proposal (1983), Ref. [8].
18. CDHS proposal, CERN/SPSC/P188 (1983).
19. E.H.M. Heijne, CERN yellow report 83-06 (1983).
20. H. Wachsmuth, private communication. We would like to thank V. Brisson for very fruitful discussions on the flux normalization and on the differential cross sections analysis.
21. R.M. Bionta, Proc. XVIIth Rencontre de Moriond, Vol. 1, 447 (1982), J. Tran Thanh Van ed.; J. van der Velde, private communication. We thank Jack van der Velde for helpful discussions on numerous aspects of the IMB experiment.
22. H. Sobel, UC Irvine, private communication. We wish to thank Hank Sobel for useful discussions on his experience with water purification systems.

23. R.M. Bionta, Proc. 1984 Fermilab Workshop on Calorimeter Calibration, to be published.
24. Nitronite model LN102, Photochemical Research Ass., Canada

FIGURE CAPTIONS

- Fig. 1 Sensitivity of ΔR to $\Delta \sin^2 \Theta_w$ as a function of γ .
 R is the ratio of differential antineutrino to neutrino cross-section:

$$R = \frac{\frac{d\sigma}{dy}(\bar{\nu})}{\frac{d\sigma}{dy}(\nu)}$$

- Fig. 2 Principle of the forward detector.
- Fig. 3 Schematic view of the test set-up.
- Fig. 4 Θ distribution for a single 20 GeV muon track.
- Fig. 5 Θ distribution for a single 15 GeV electron event.
- Fig. 6a Angular distribution for 15 GeV electrons.
- Fig. 6b Angular distribution for 5 GeV electrons.
- Fig. 7a σ of the angular distribution of electrons events as a function of electron energy.
- Fig. 7b Fractions of events outside of 2σ for electron events as a function of electron energy.
- Fig. 8 Number of photoelectrons detected in the focal plane per GeV for different energies of the electron.
- Fig. 9 Θ distribution for a single 15 GeV pion event.

- Fig. 10 Number of photoelectrons detected in the first column of the shower scanner for electrons and converted γ 's of 10 GeV energy.
- Fig. 11 Electron- γ separation vs. survival rate of electrons of 10 GeV energy.
- Fig. 12 Number of photoelectrons detected in the focal plane for electrons and pions of 10 GeV.
- Fig. 13 Expected $E\theta^2$ distribution for $\nu_{\mu}e$ signal and background in the neutrino beam.
- Fig. 14 As fig. 13 with coarser $E\theta^2$ bins.
- Fig. 15 Expected $E\theta^2$ distribution for $\bar{\nu}_{\mu}e$ signal and background in the antineutrino beam.
- Fig. 16 As fig. 15 with coarser $E\theta^2$ bins.
- Fig. 17 Layout of the experiment in the BEBC hall.
- Fig. 18 Transversal and longitudinal cuts of the detector.
- Fig. 19 Drawing of a photomultiplier with housing of the IMB detector.
- Fig. 20 Schematic layout of the shower scanner.
- Fig. 21 Computer simulations of the Cerenkov cone imaging.

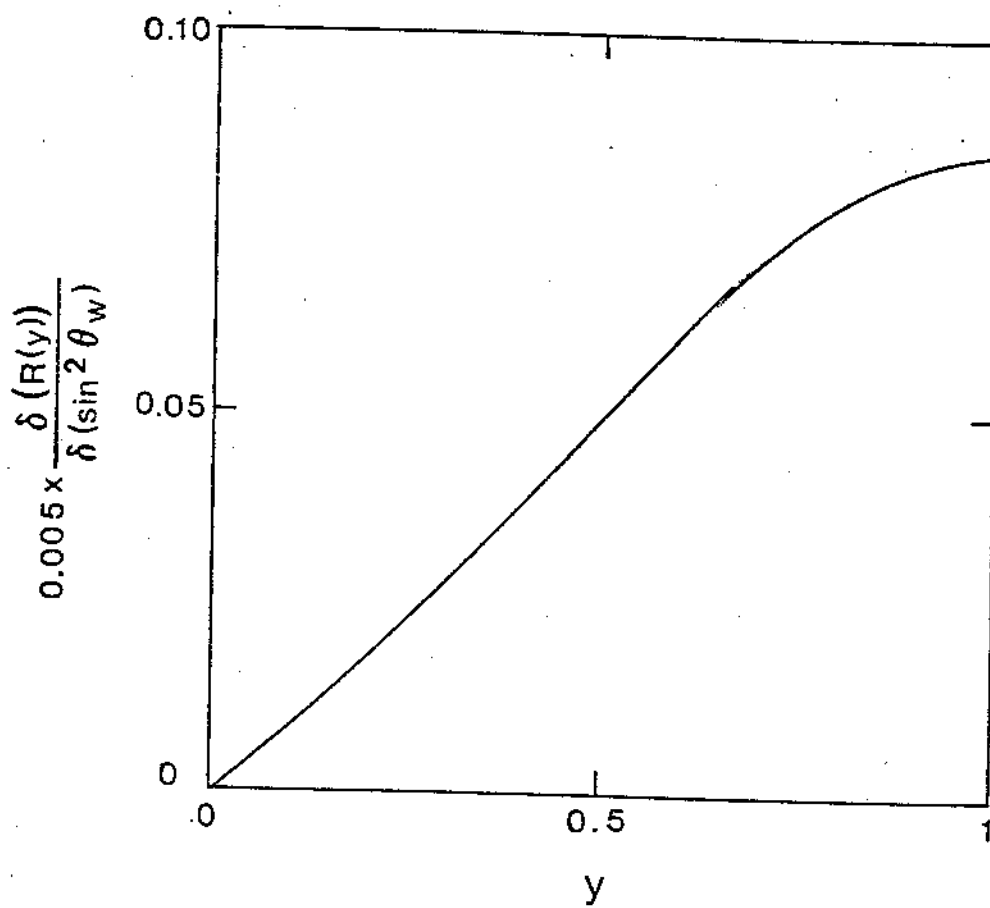


Fig. 1 Sensitivity of ΔR to $\Delta \sin^2 \theta_w$ as a function of y .

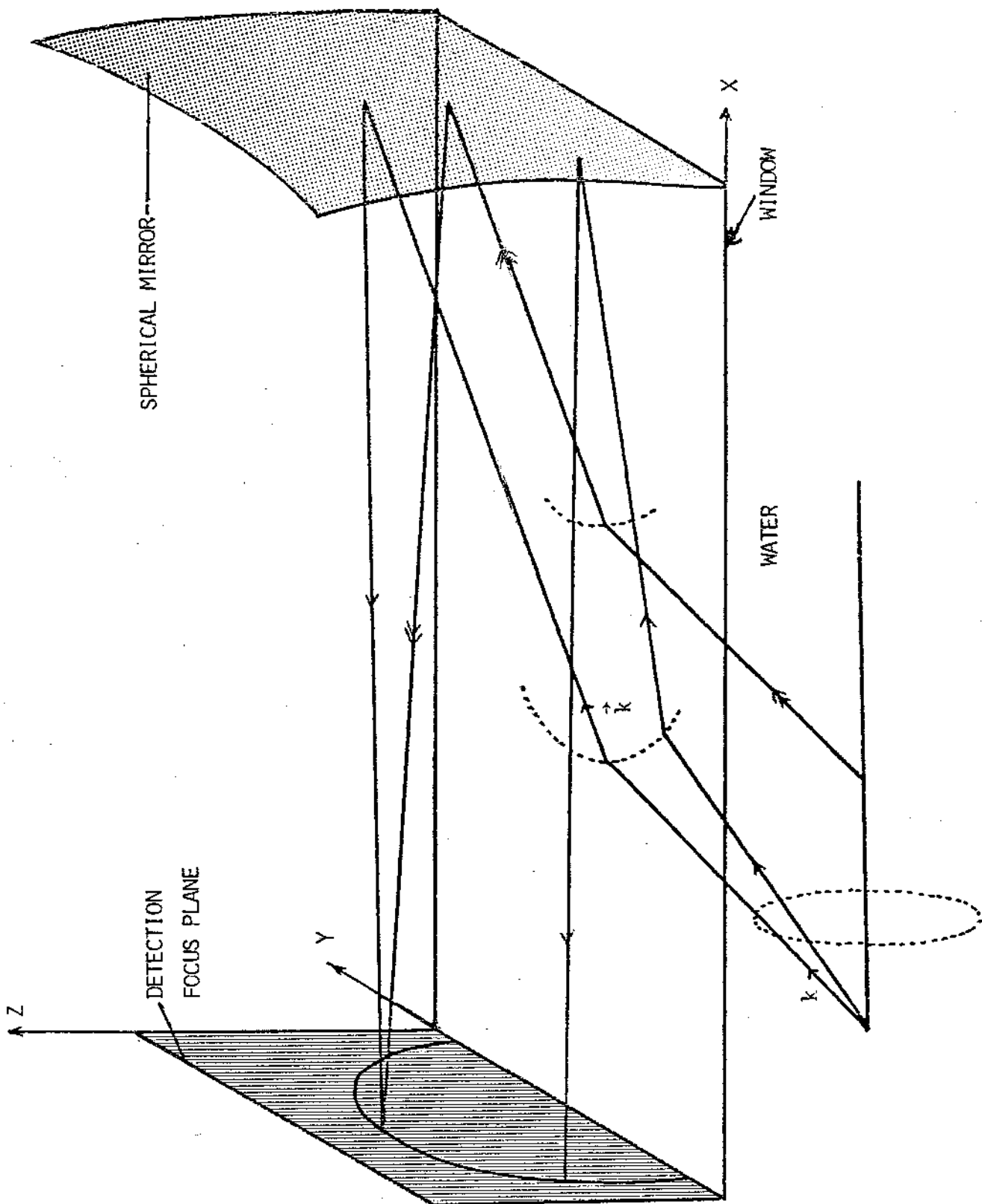


Fig. 2 Principle of the forward detector.

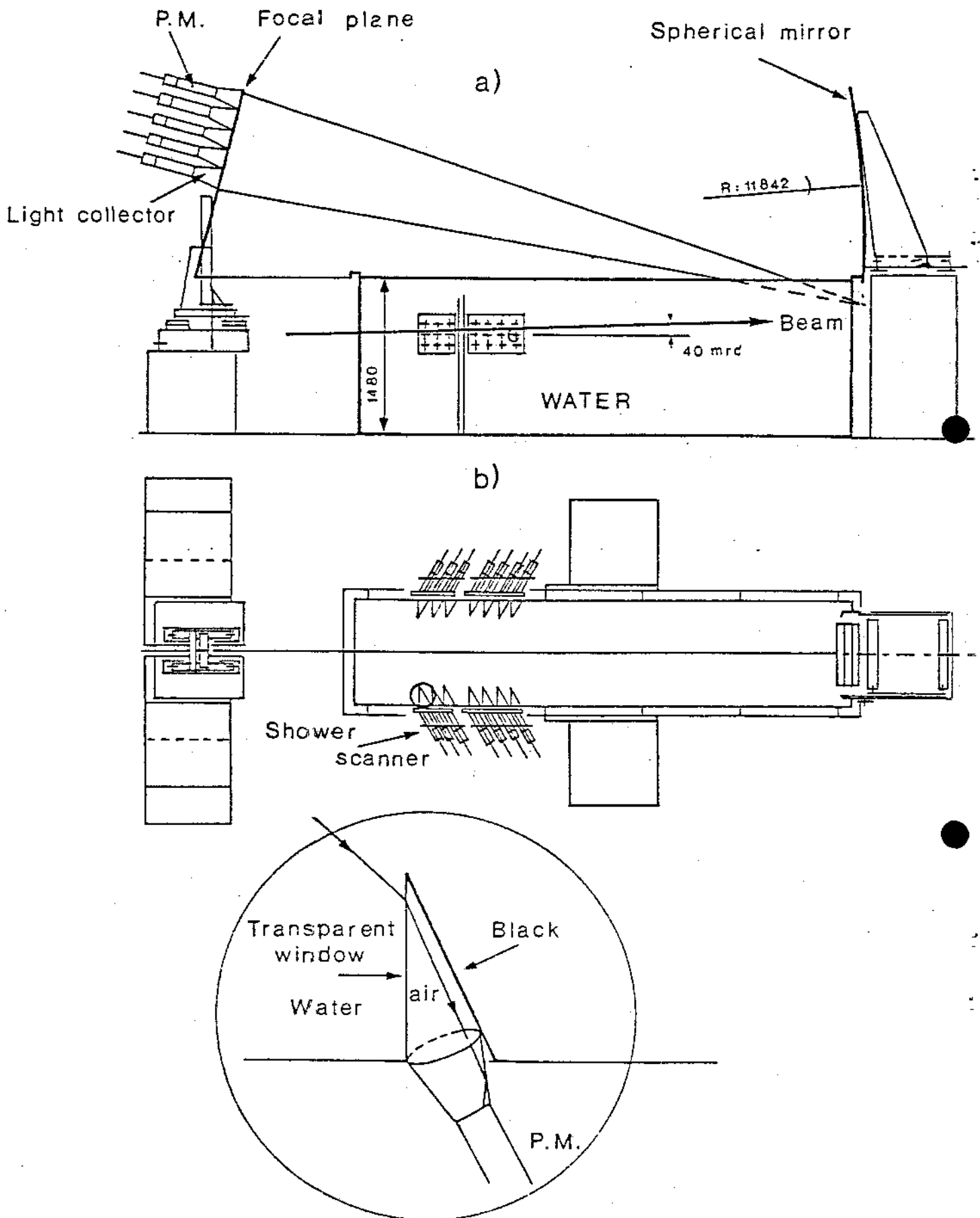


Fig. 3 Schematic view of the test set-up.

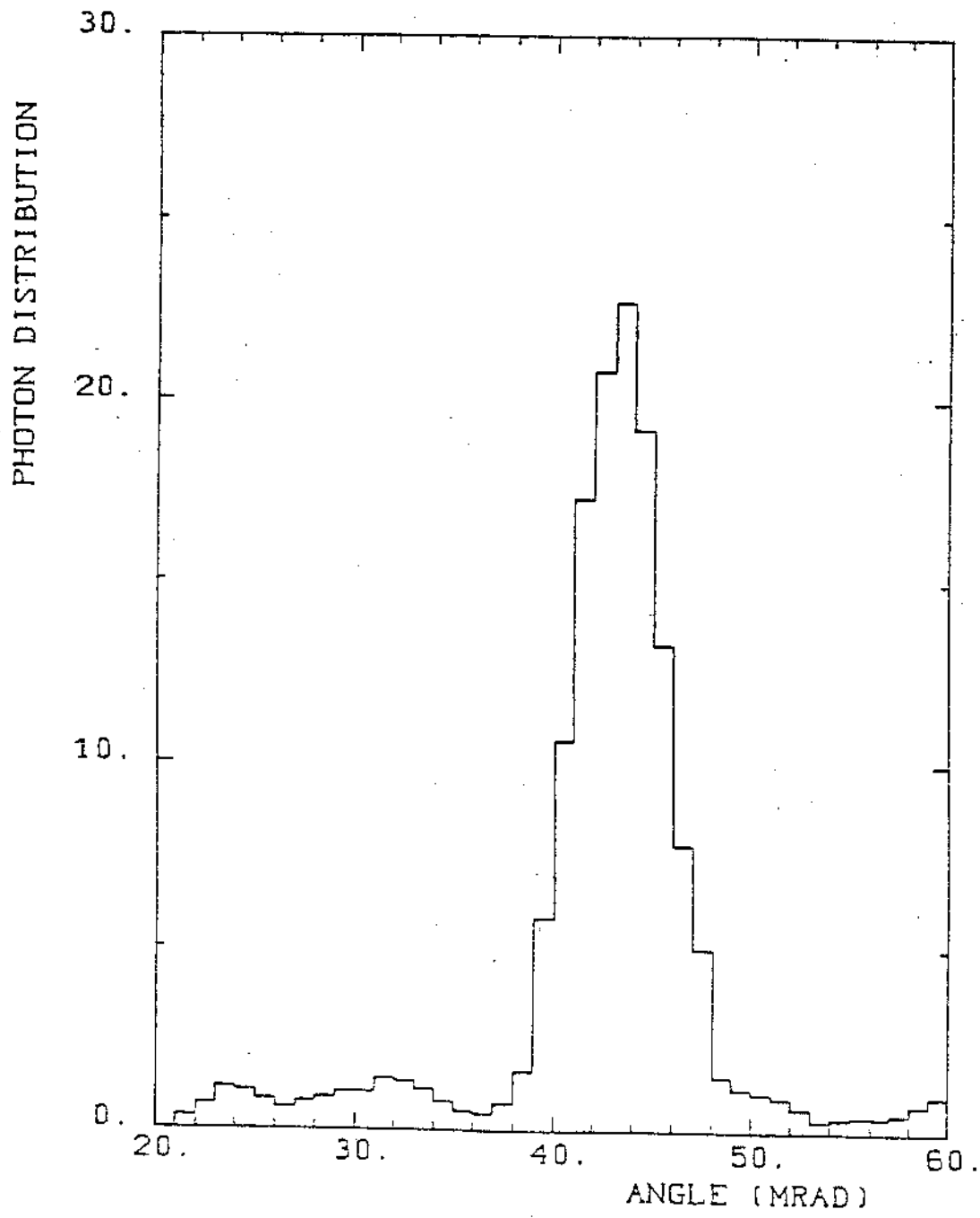


Fig. 4 Θ distribution for a single 20 GeV muon track.

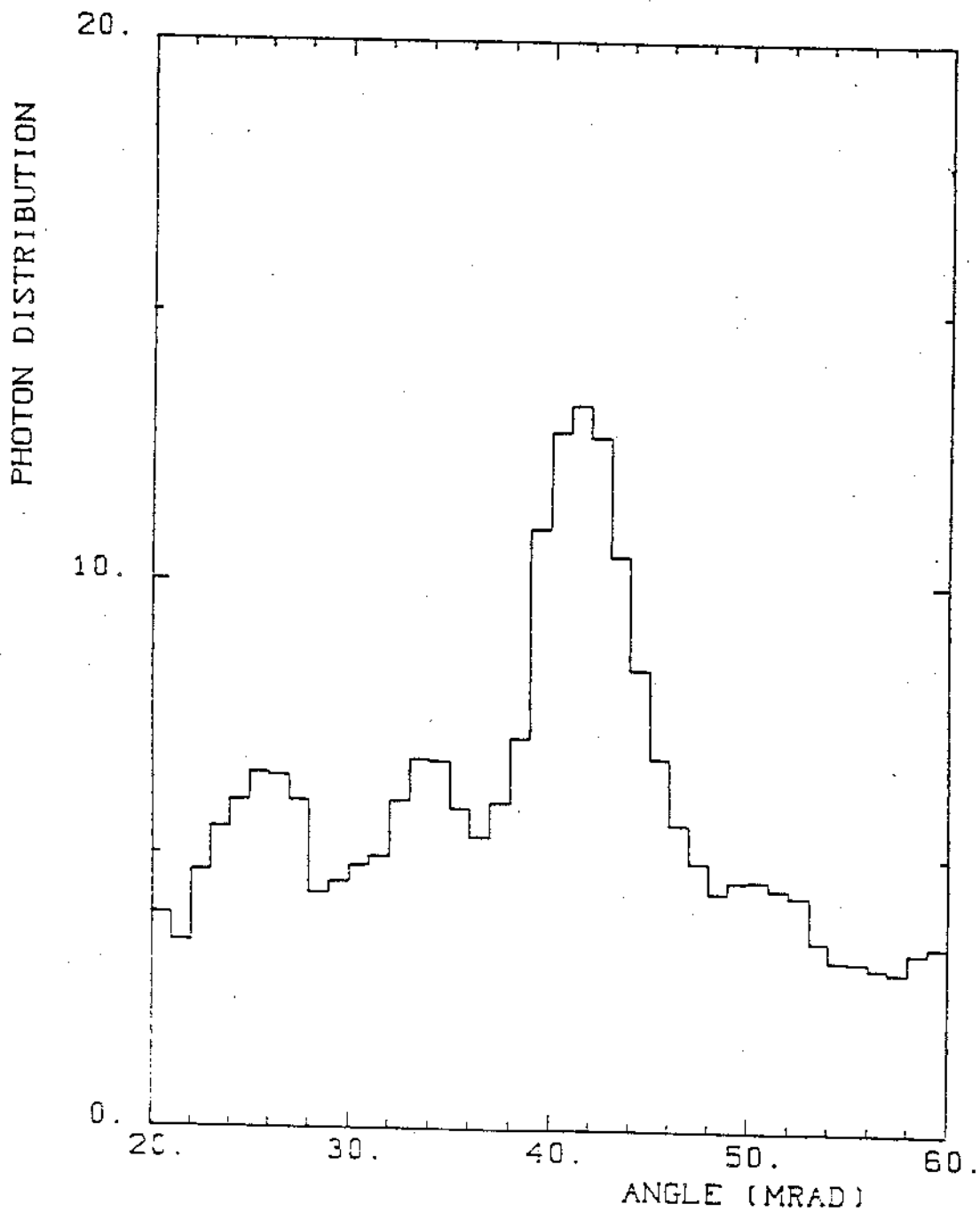


Fig. 5 Θ distribution for a single 15 GeV electron event.

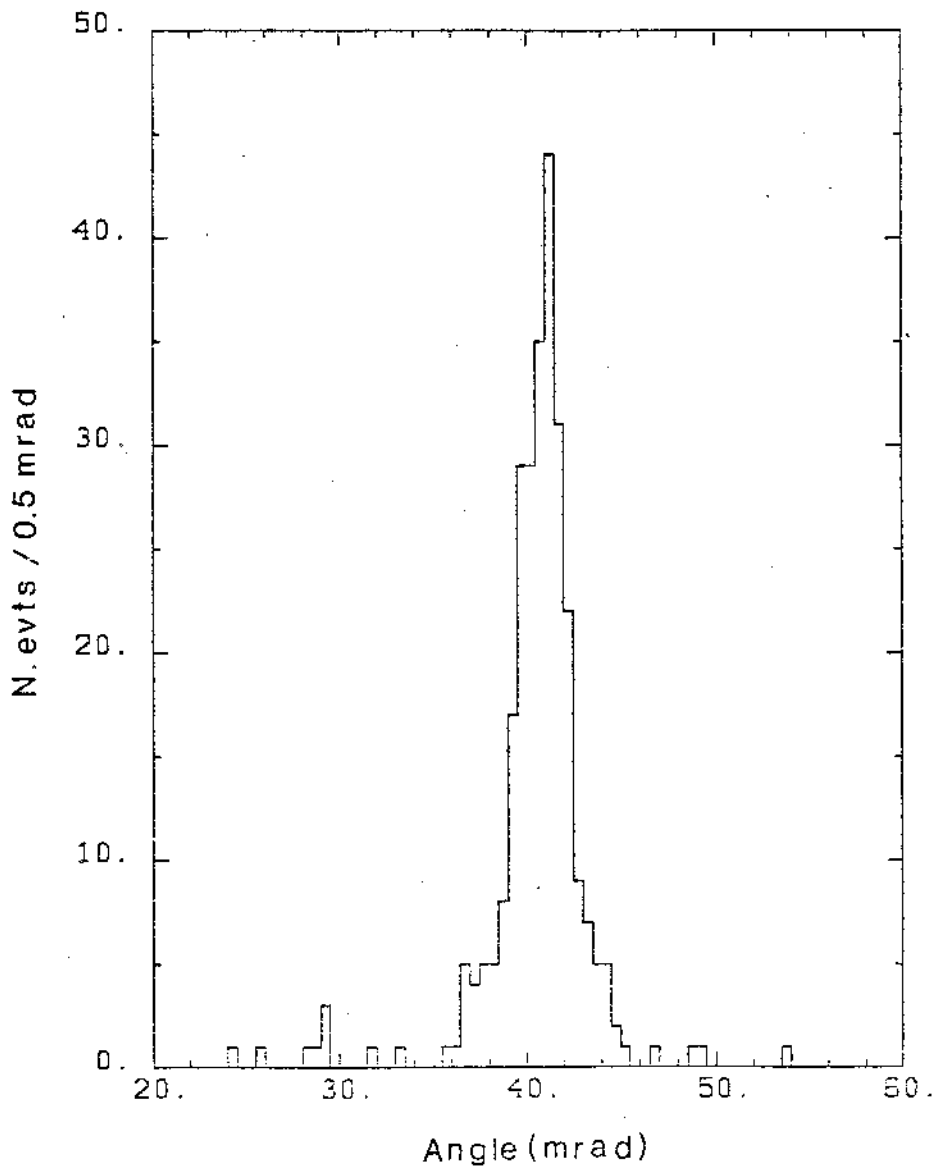


Fig. 6a Angular resolution for 15 GeV electrons

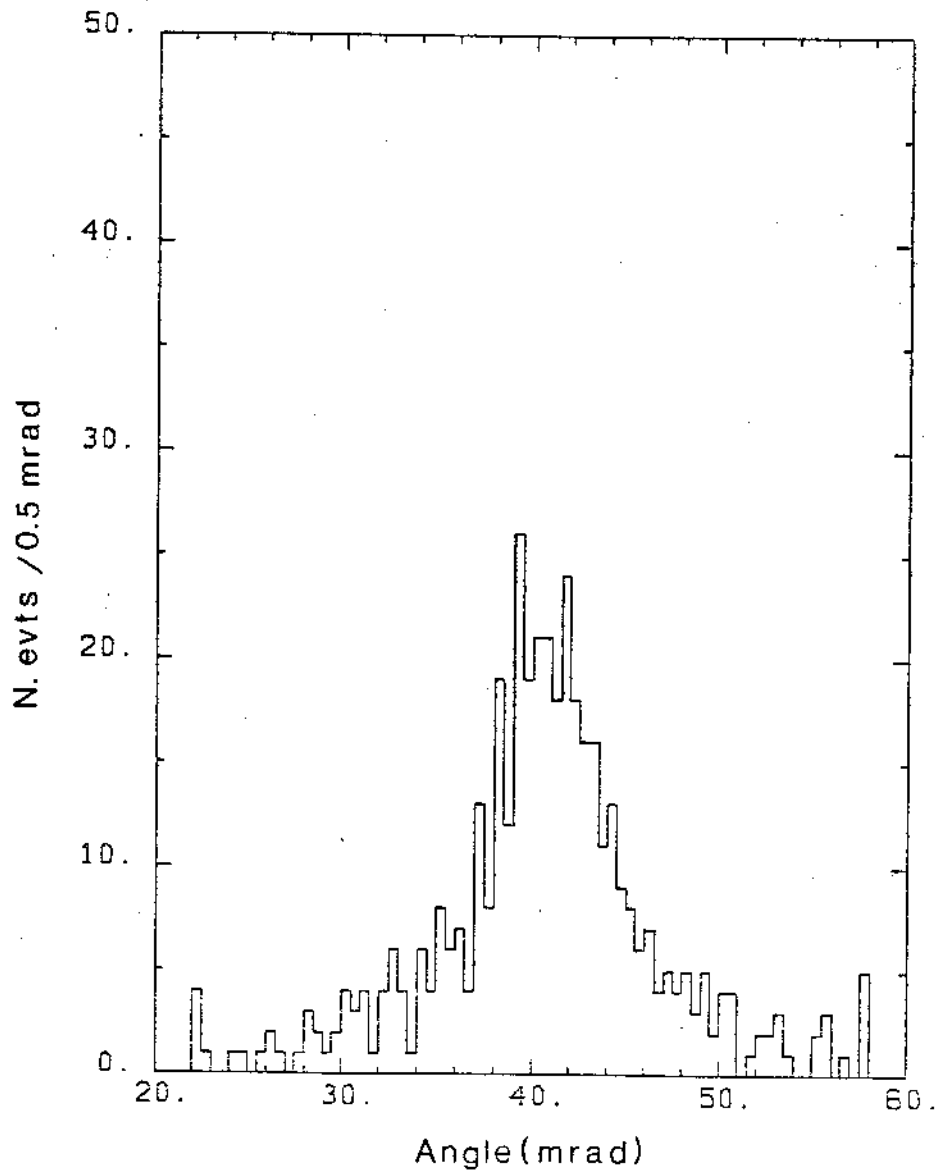


Fig. 6b Angular resolution for 5 GeV electrons

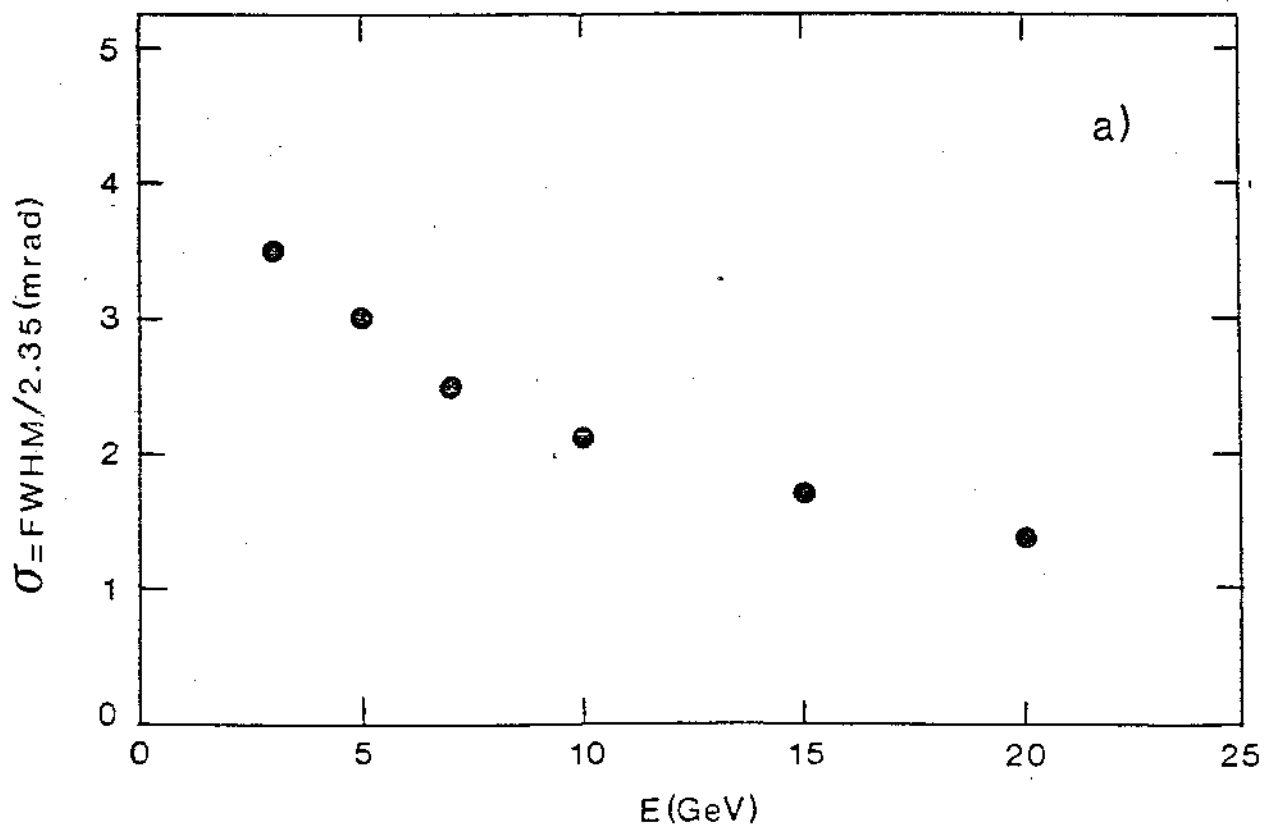
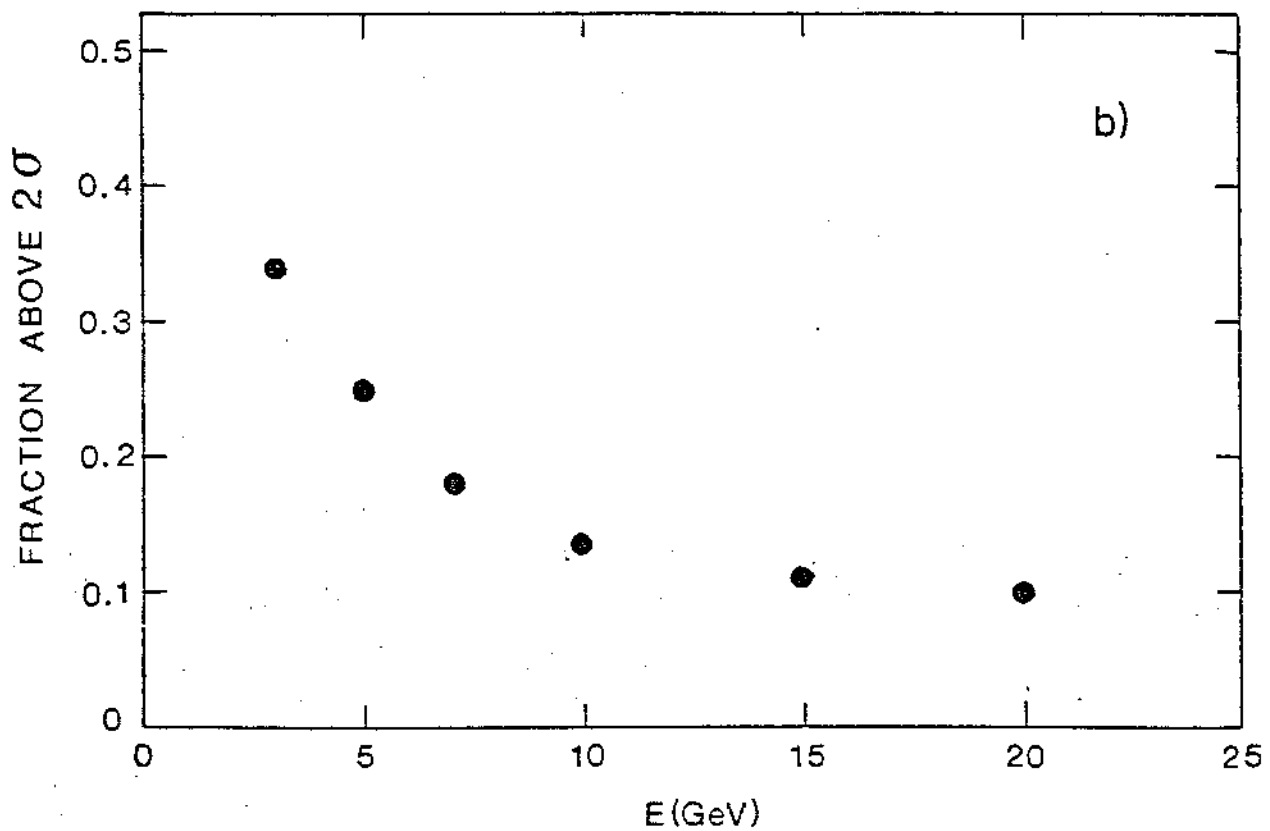


Fig. 7a σ of the angular distribution of electrons events as a function of electron energy.

Fig. 7b Fractions of events outside of 2σ for electron events as a function of electron energy.

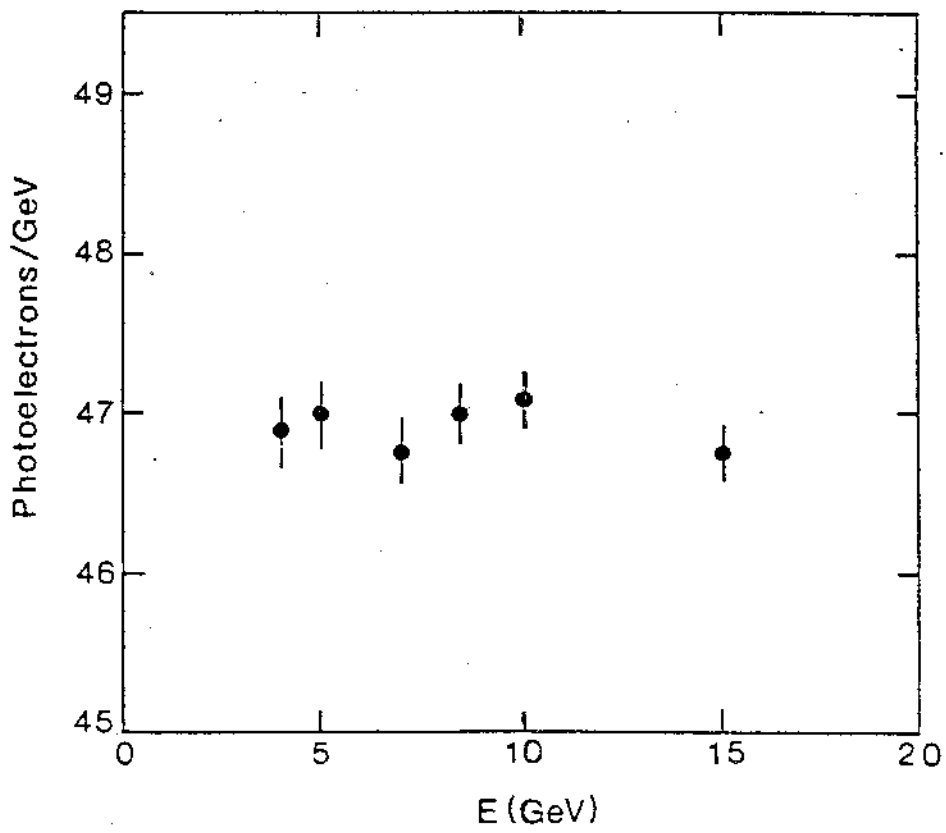


Fig. 8 Number of photoelectrons detected in the focal plane per GeV for different energies of the electron.

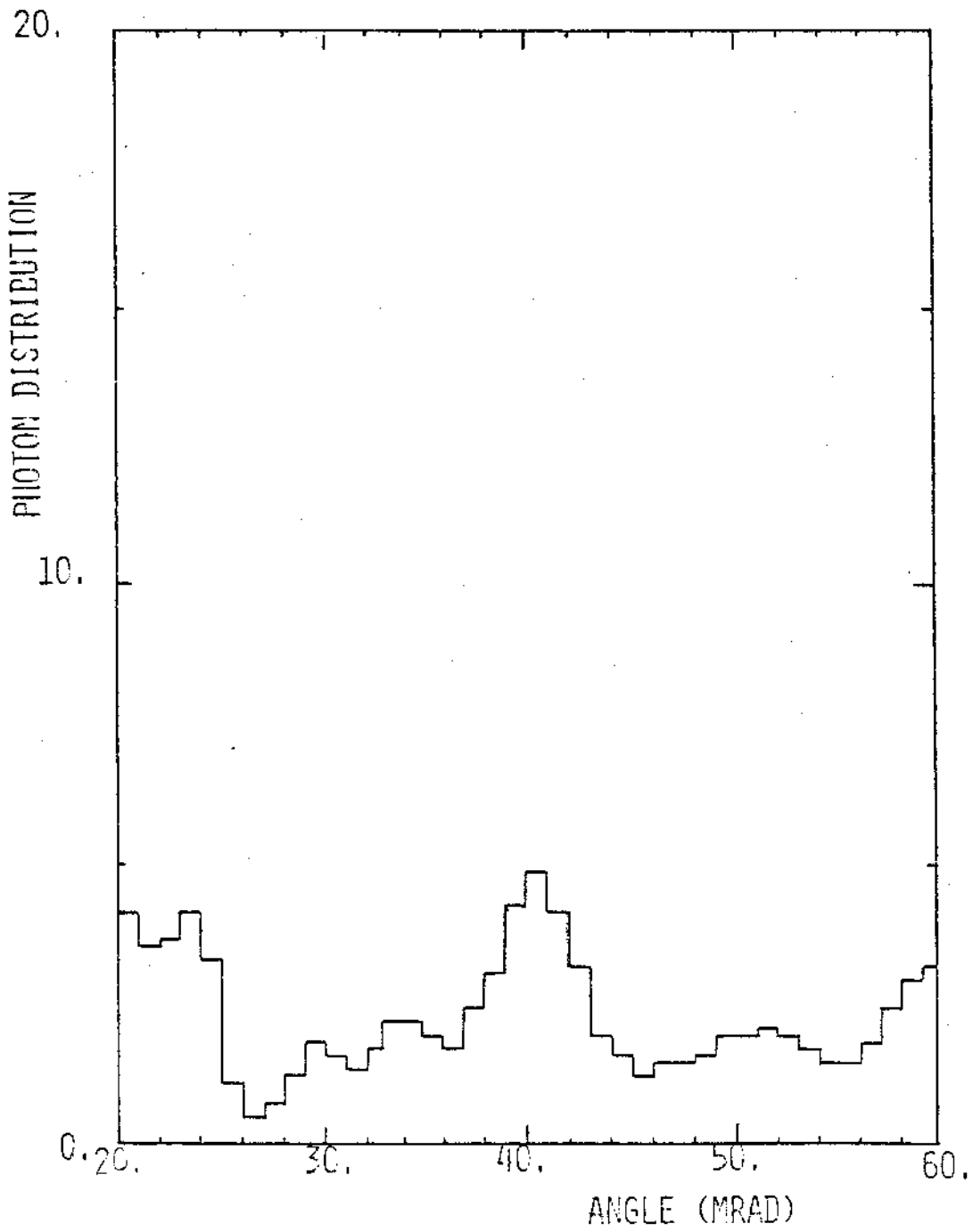


Fig. 9 Θ distribution for a single 15 GeV pion event.

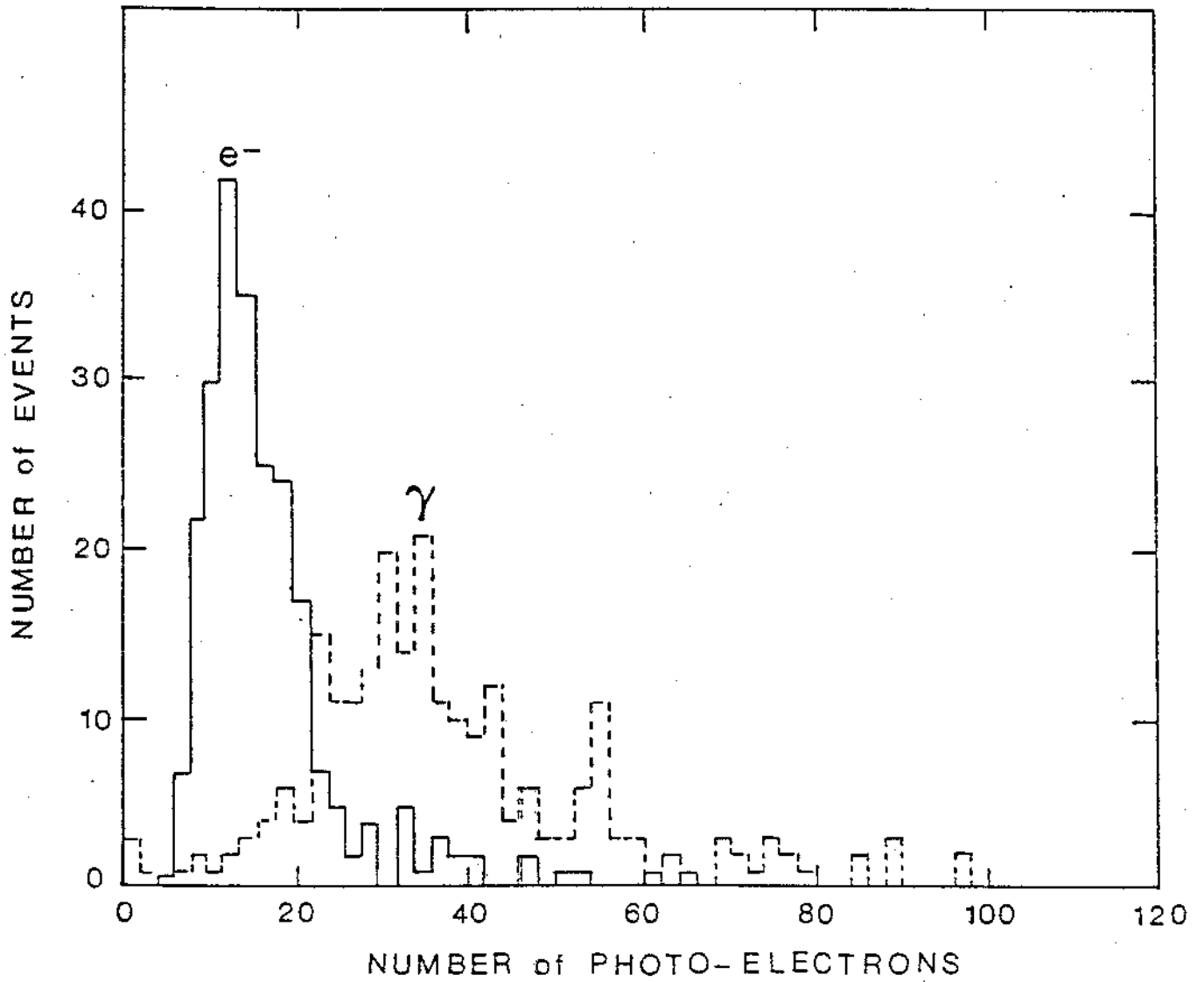
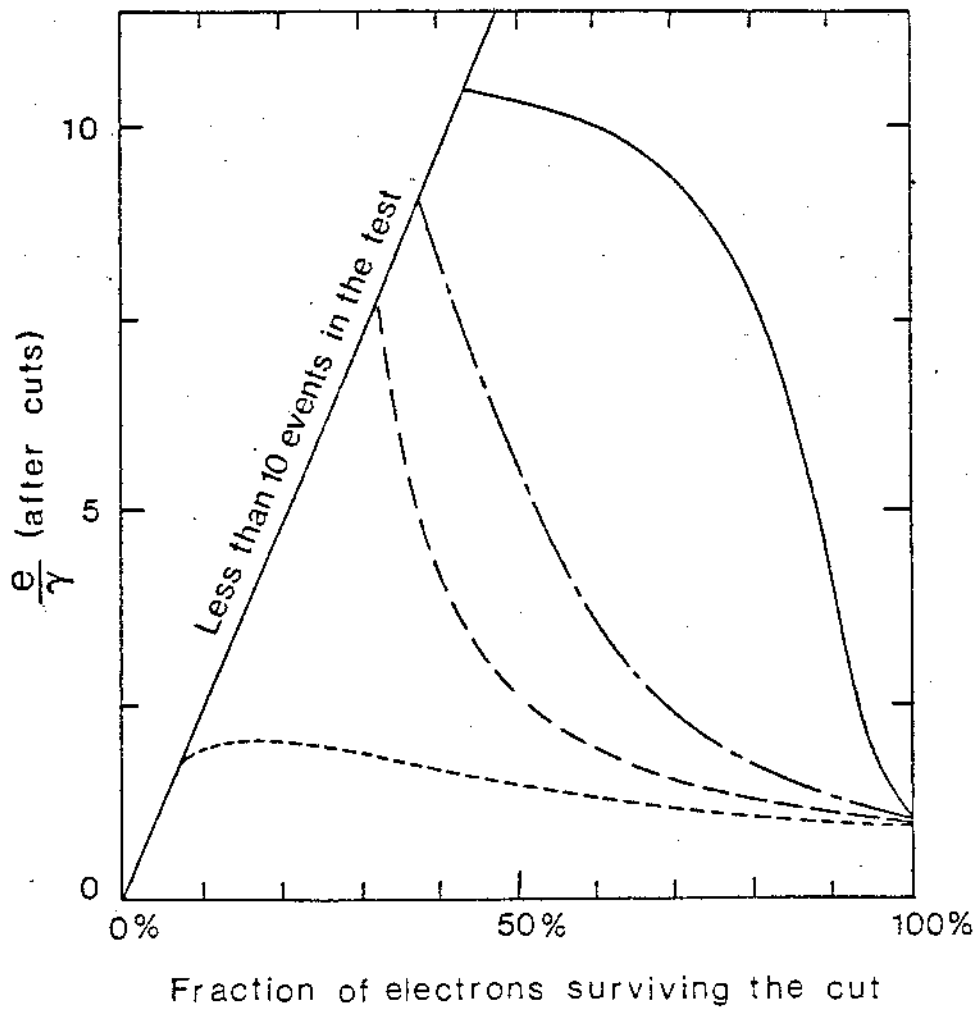


Fig. 10 Number of photoelectrons detected in the first column of the shower scanner for electrons and converted γ 's of 10 GeV energy.



- shower scanned after $\frac{1}{12}$ of X_0 over $\frac{1}{6} X_0$
- - - " " $\frac{1}{4}$ of X_0 over $\frac{1}{3} X_0$
- · - · " " $\frac{7}{12}$ of X_0 over $\frac{1}{3} X_0$
- · · · " " $\frac{5}{4}$ of X_0 over $\frac{1}{3} X_0$

Fig. 11 Electron- γ separation vs. survival rate of electrons of 10 GeV energy.

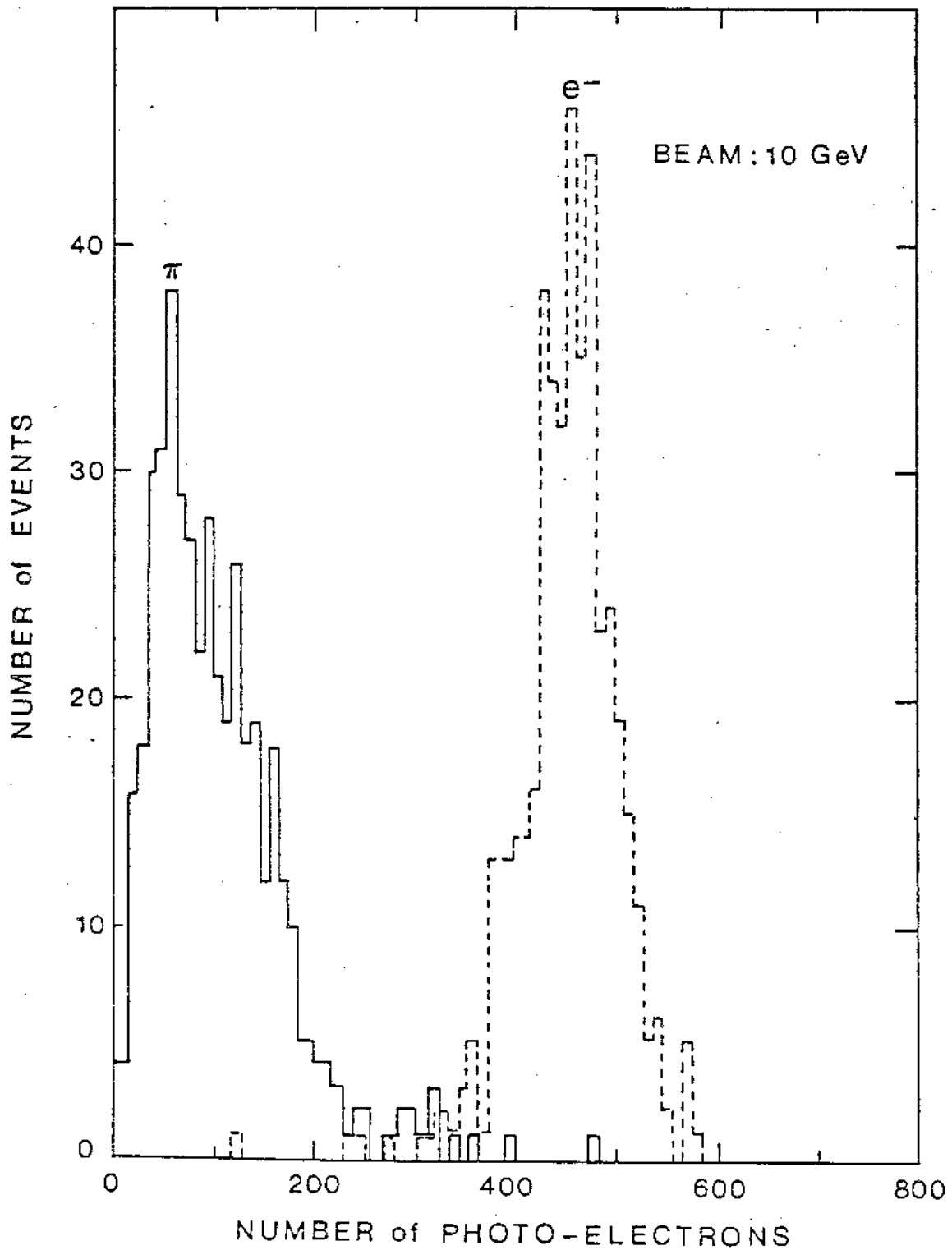


Fig. 12 Number of photoelectrons detected in the focal plane for electrons and pions of 10 GeV.

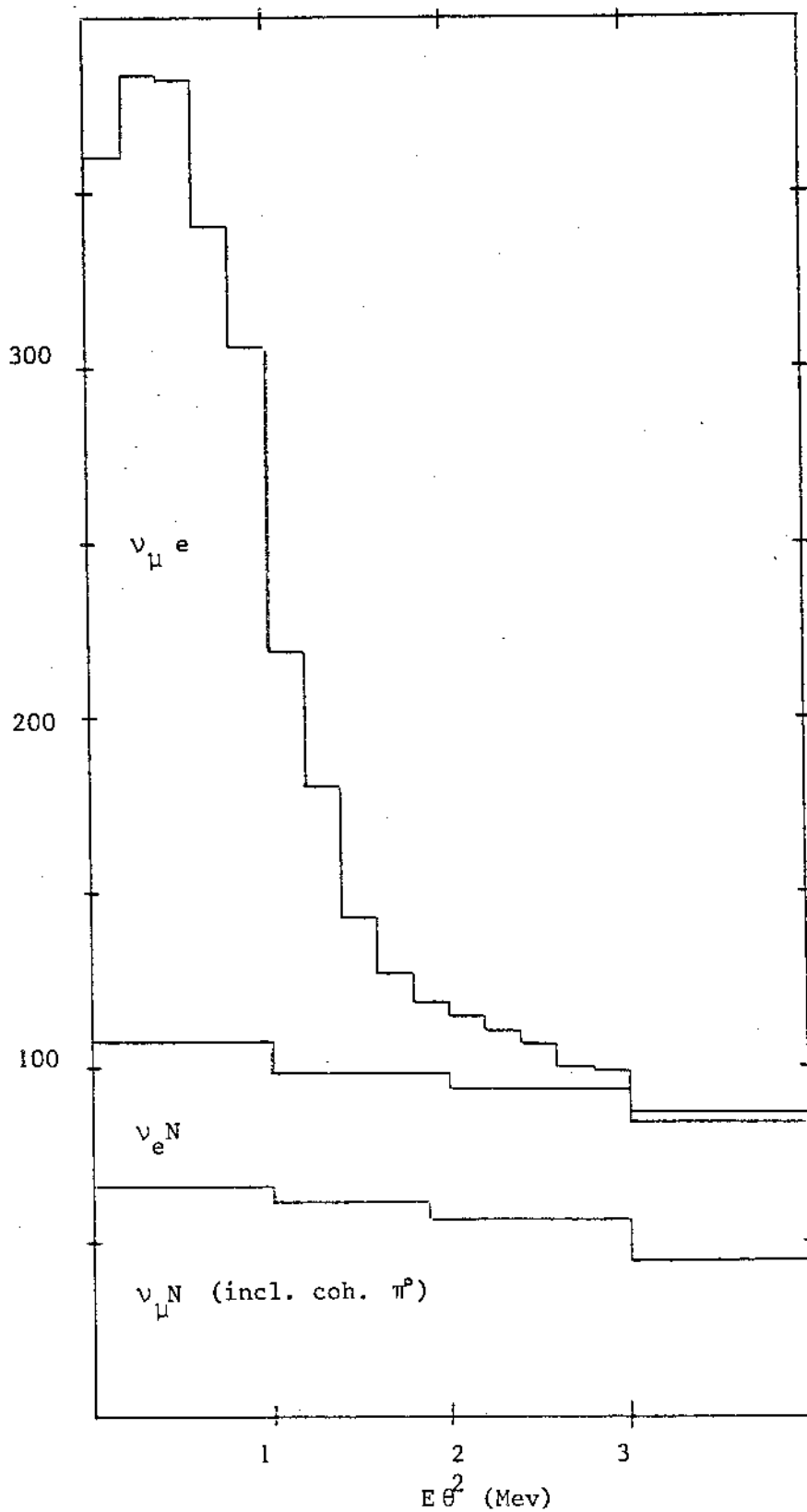


Fig. 13 Expected $E\theta^2$ distribution for $\nu_{\mu}e$ signal and background in the neutrino beam.

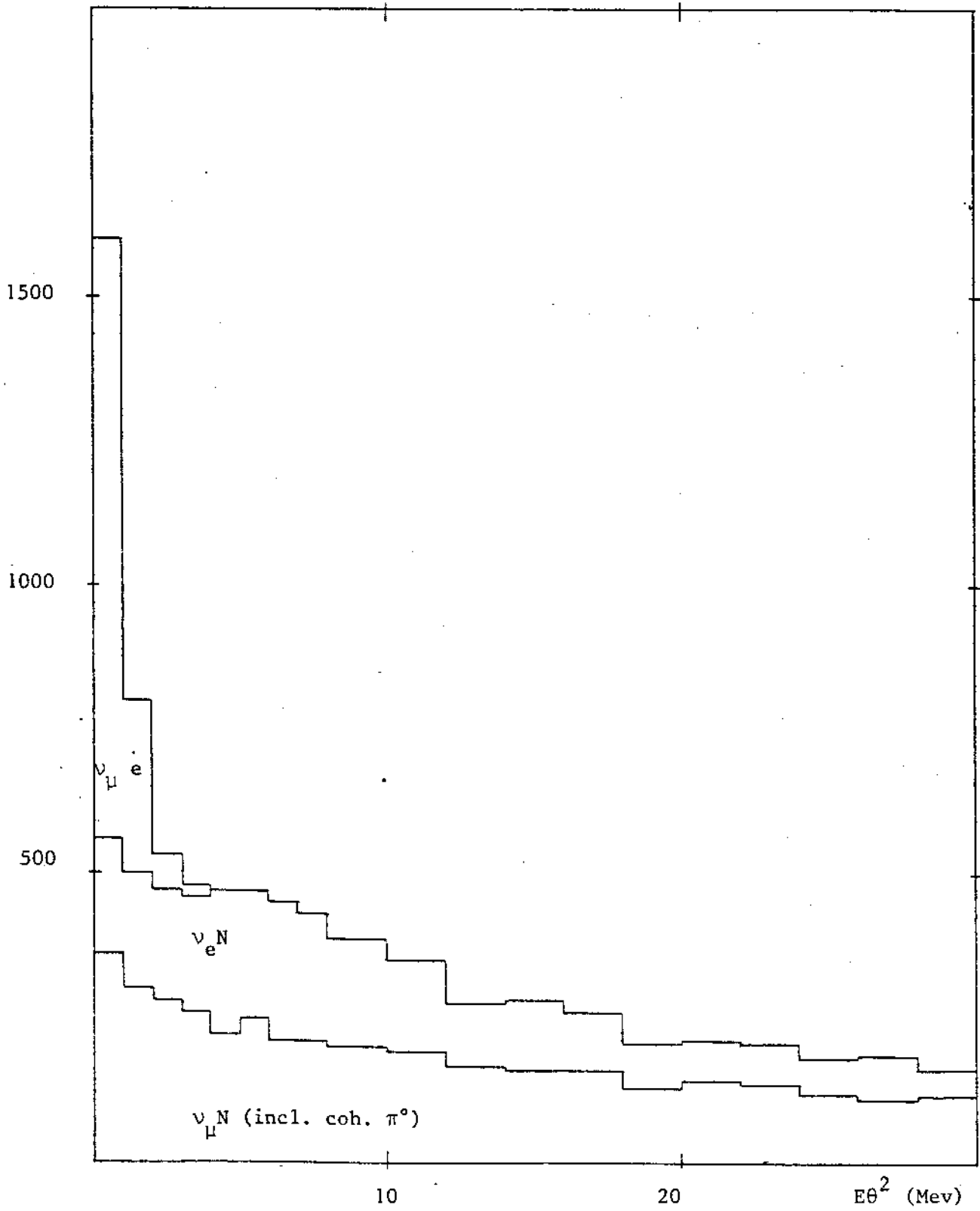


Fig. 14 As fig. 13 with coarser $E\theta^2$ bins.

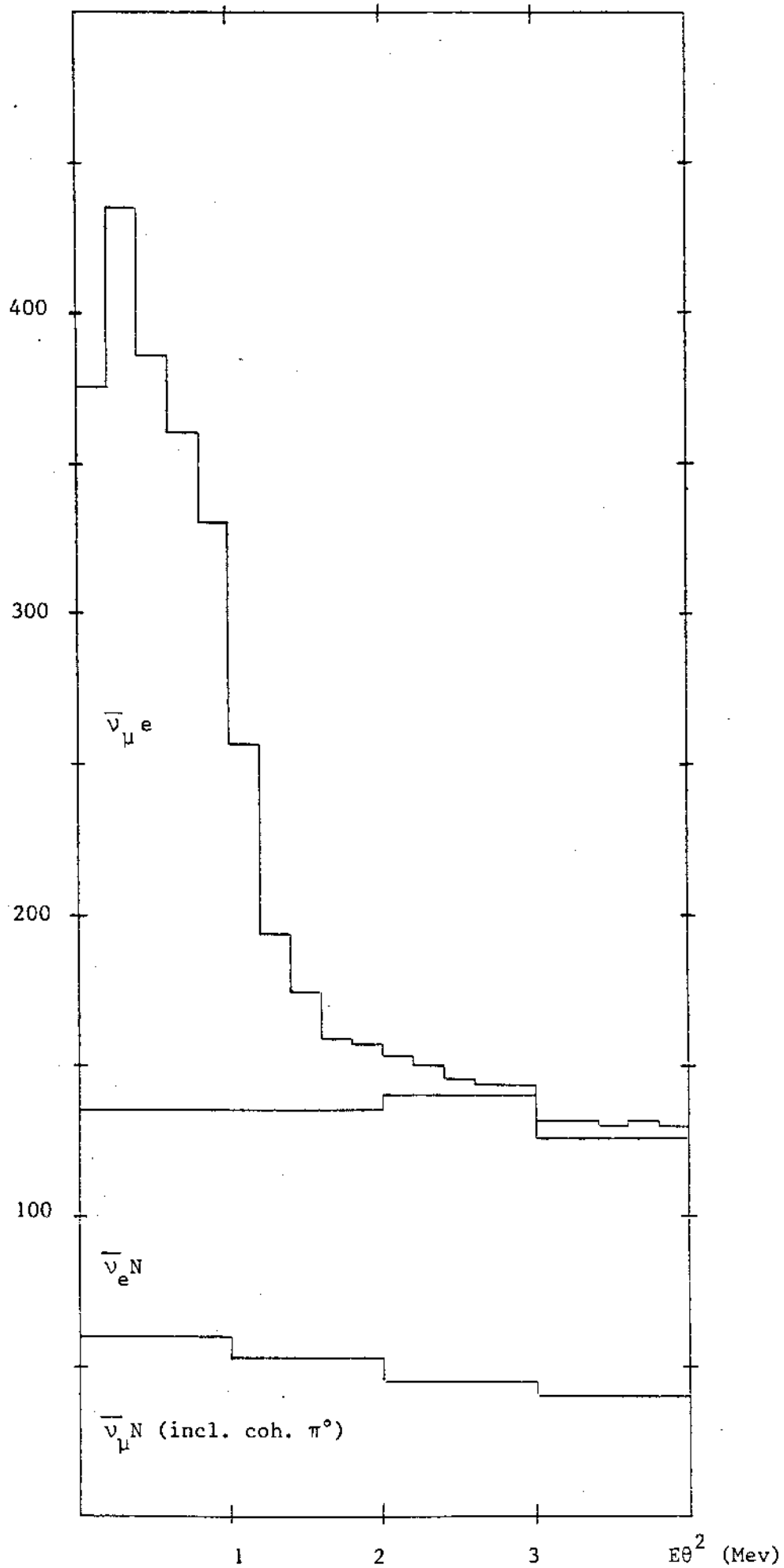


Fig. 15 Expected $E\theta^2$ distribution for $\bar{\nu}_{\mu}e$ signal and background in the antineutrino beam

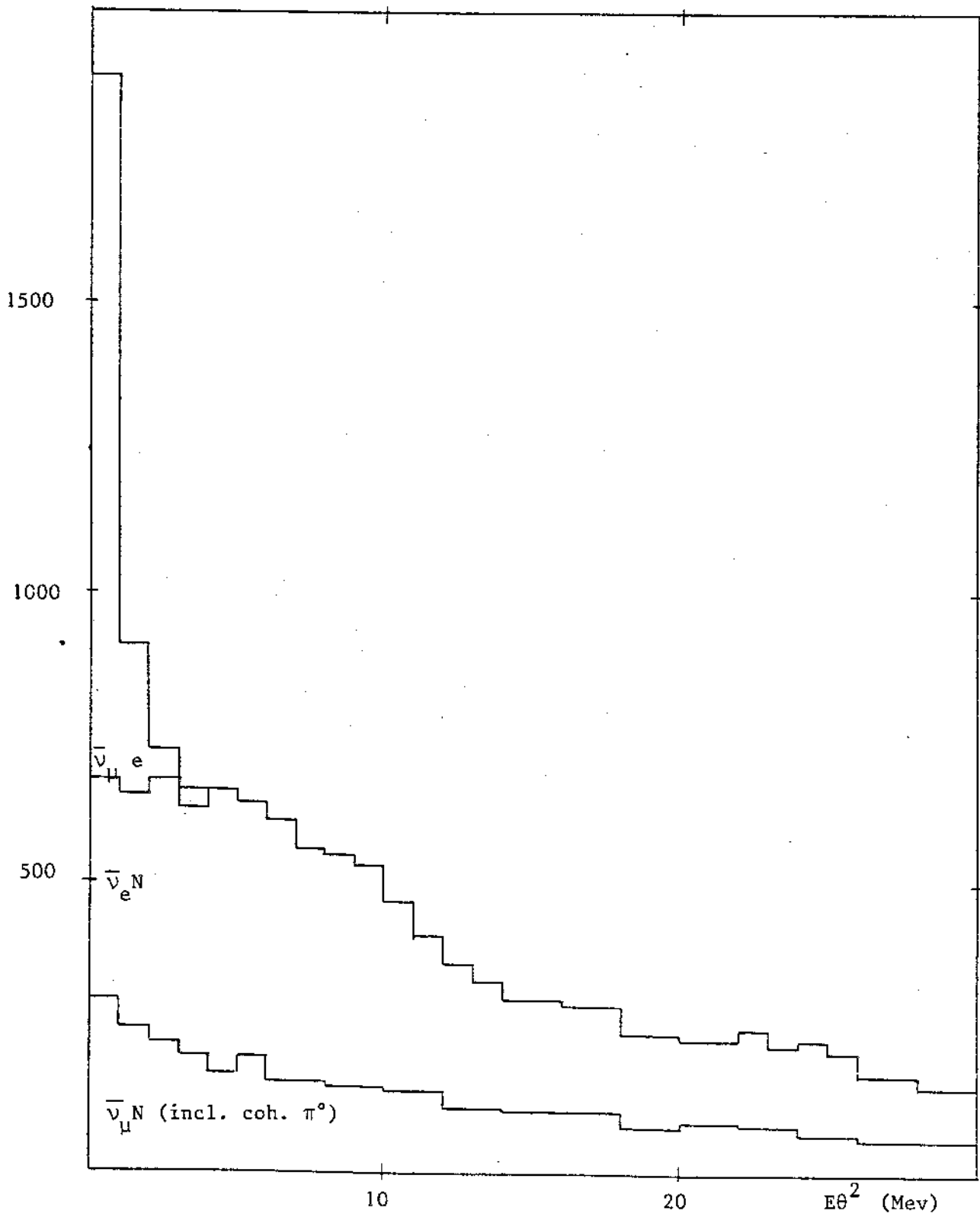


Fig. 16 As fig. 15 with coarser $E\theta^2$ bins.

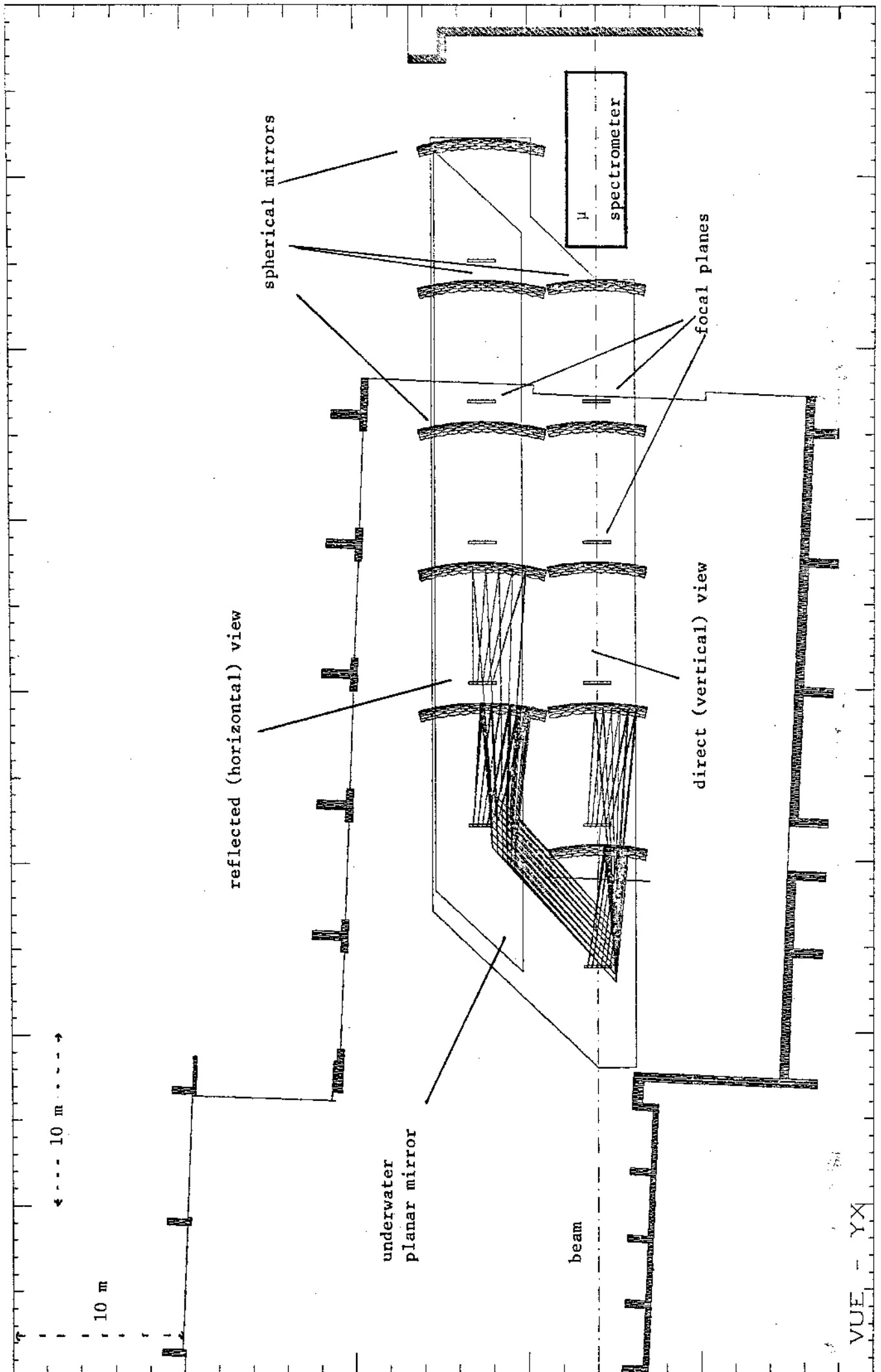


Fig. 17 Layout of the experiment in the BEBC hall.

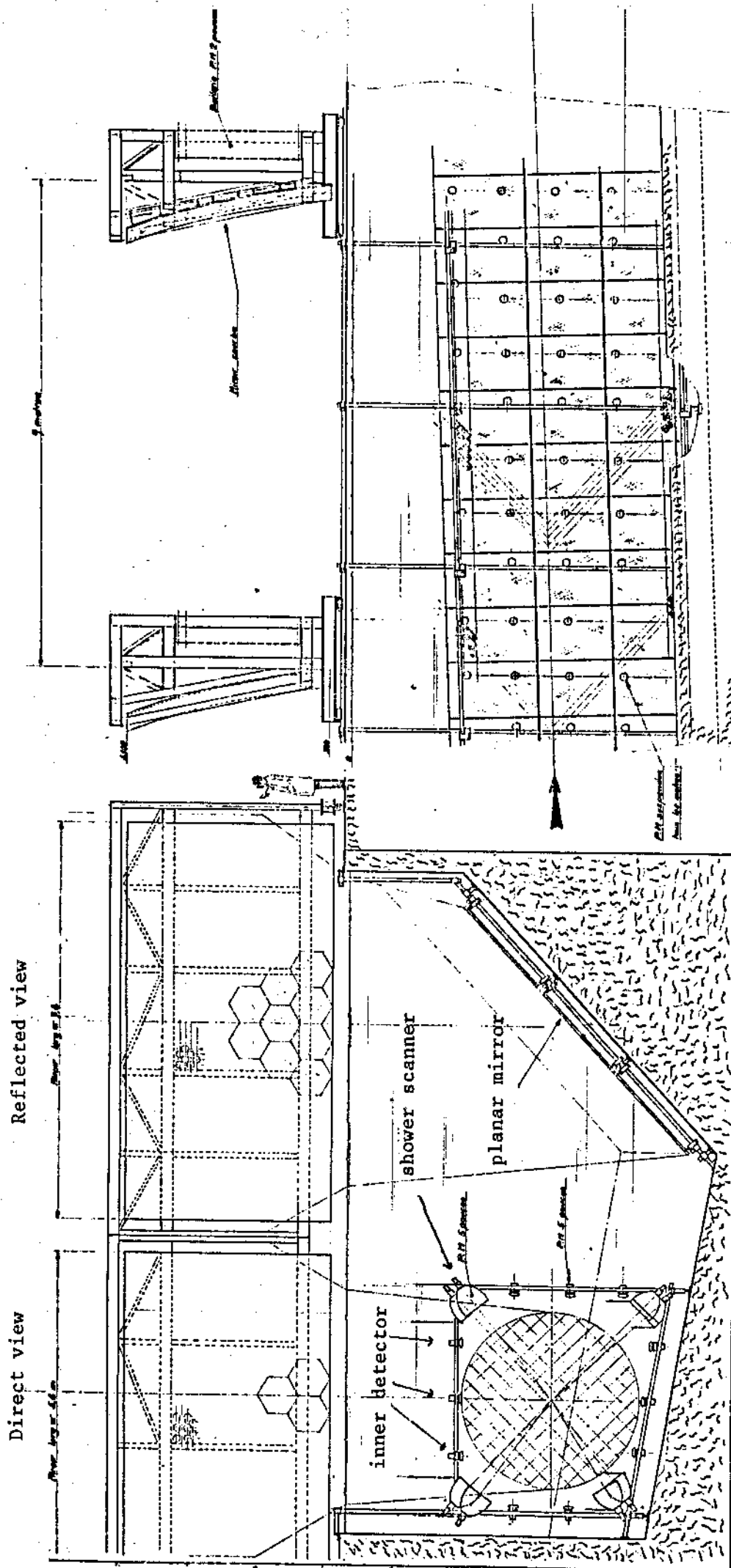


Fig. 18 Transversal and longitudinal cuts of the detector.

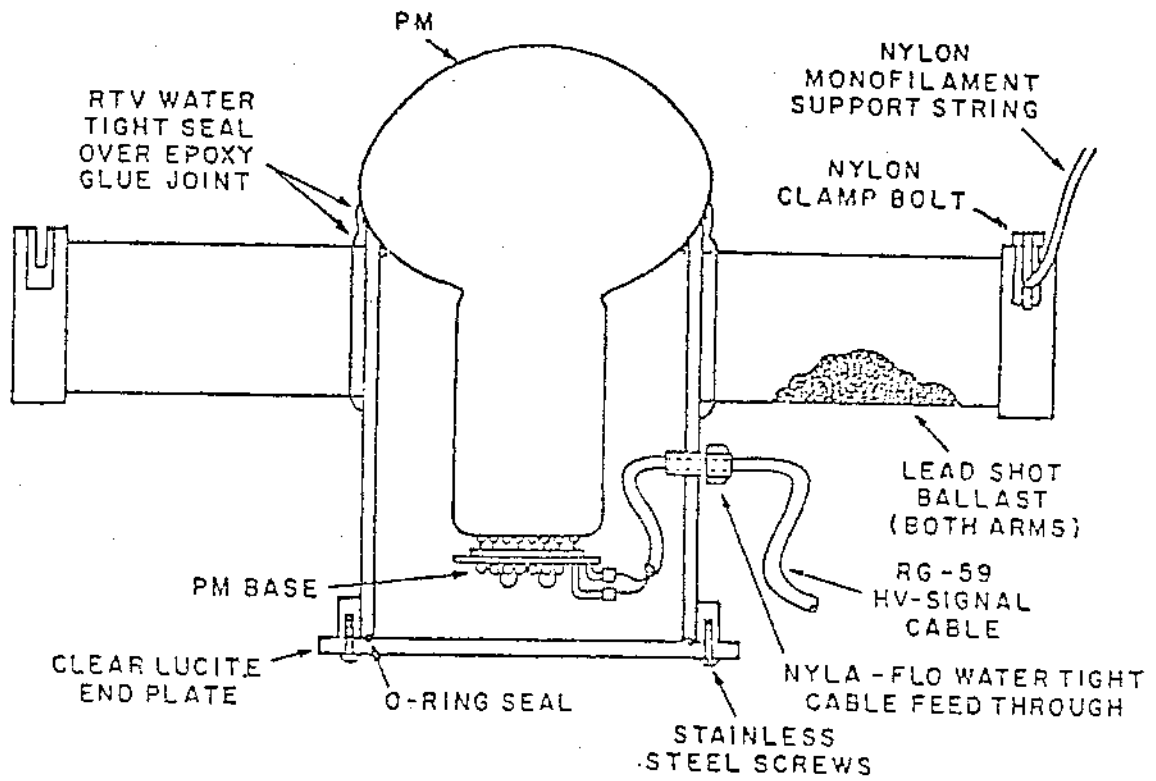


Fig. 19 Drawing of a photomultiplier with housing of the IMB detector.

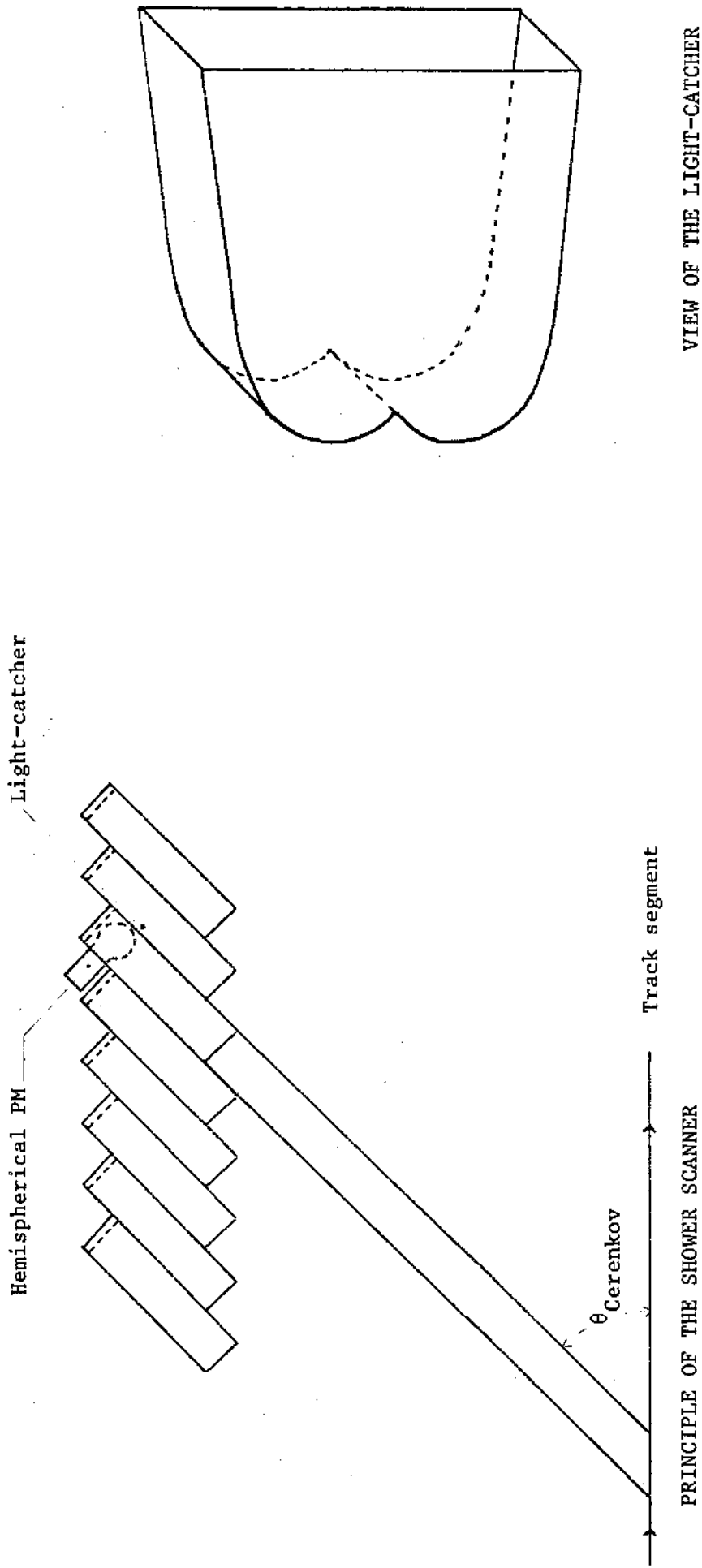


Fig. 20 Schematic layout of the shower scanner.

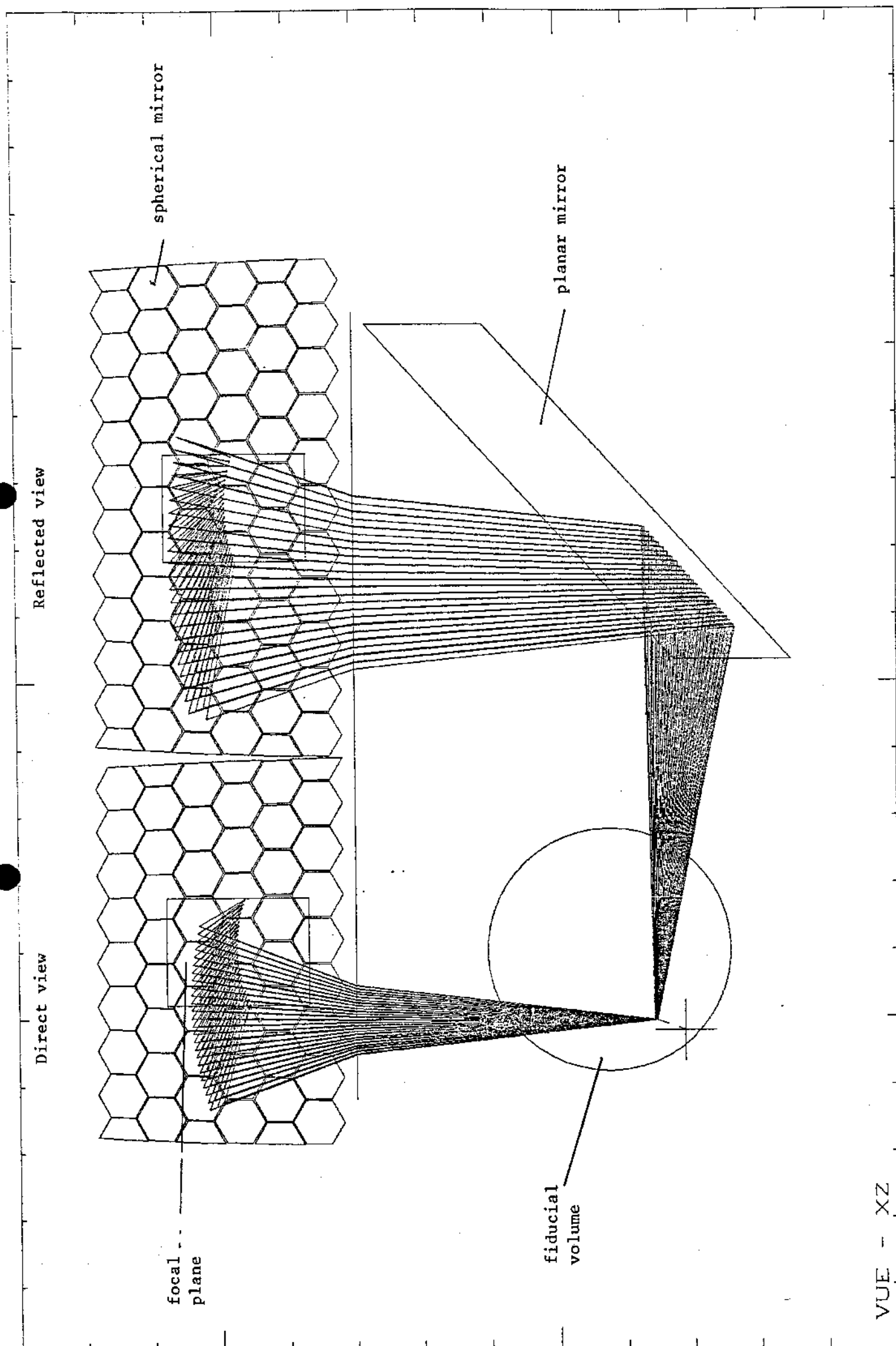


FIG. 21 A OPTICAL SYSTEM OF THE DETECTOR - TRANSVERSE CUT

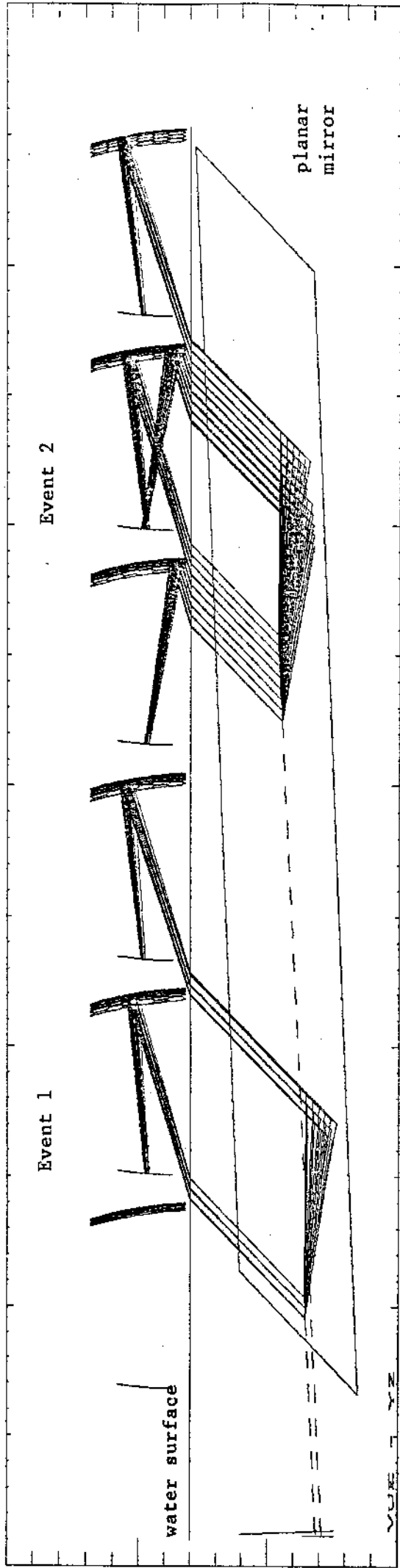


FIG. 21 C SIDE VIEW OF THE DETECTOR

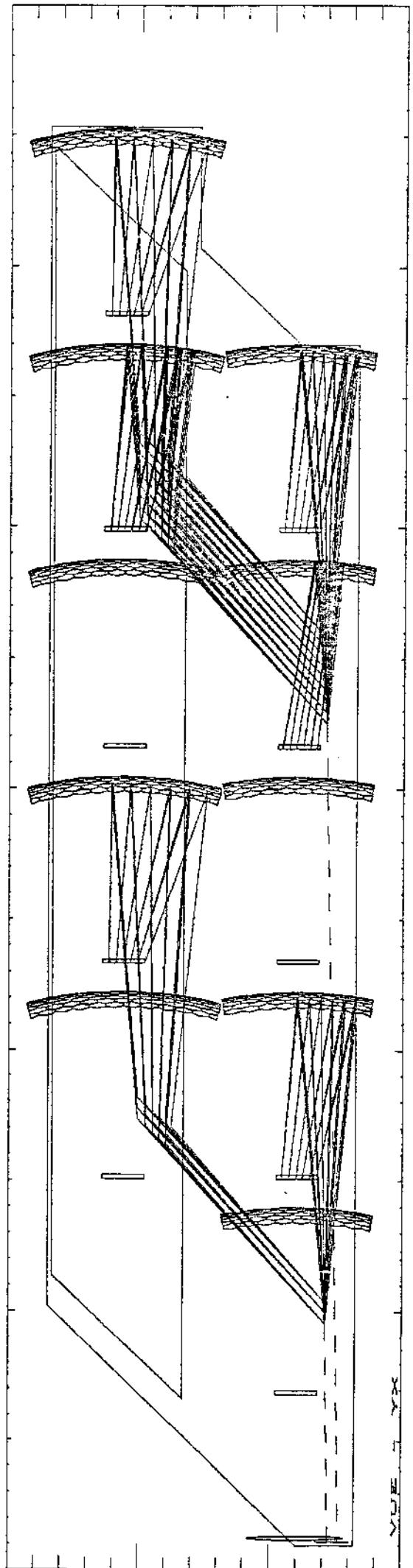
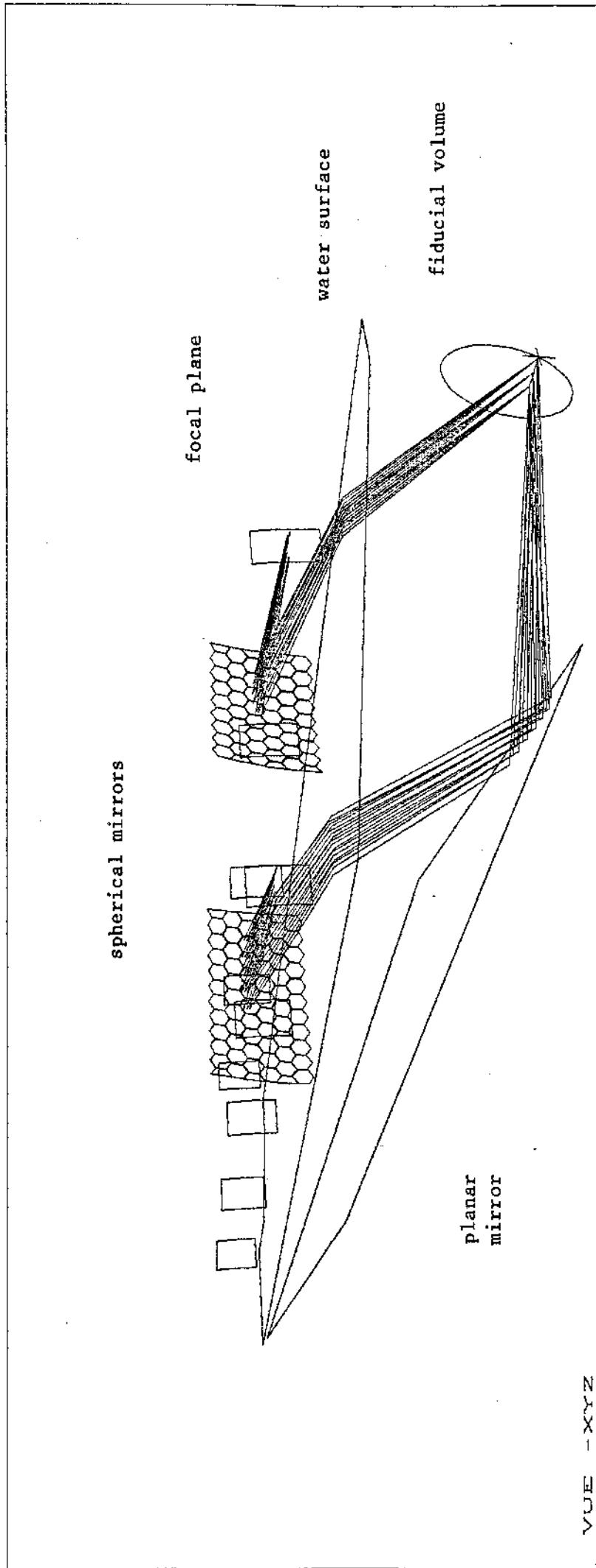


FIG. 21 B TOP VIEW OF THE DETECTOR



VUE -XYZ

FIG. 21 D ARTISTS VIEW